

# Precision radial velocity measurements by the forward-modeling technique in the near-infrared

\*

Teruyuki HIRANO<sup>1</sup>, Masayuki KUZUHARA<sup>2,3</sup>, Takayuki KOTANI<sup>2,3,4</sup>, Masashi OMIYA<sup>2,3</sup>, Tomoyuki KUDO<sup>5</sup>, Hiroki HAKAWA<sup>5</sup>, Sébastien VIEVARD<sup>2,5</sup>, Takashi KUROKAWA<sup>2,6</sup>, Jun NISHIKAWA<sup>2,3</sup>, Motohide TAMURA<sup>2,3,7</sup>, Klaus HODAPP<sup>8</sup>, Masato ISHIZUKA<sup>7</sup>, Shane JACOBSON<sup>8</sup>, Mihoko KONISHI<sup>9</sup>, Takuma SERIZAWA<sup>6</sup>, Akitoshi UEDA<sup>3</sup>, Eric GAIDOS<sup>10</sup> and Bun'ei SATO<sup>1</sup>

<sup>1</sup>Department of Earth and Planetary Sciences, Tokyo Institute of Technology, 2-12-1 Ookayama, Meguro-ku, Tokyo 152-8551, Japan

<sup>2</sup>Astrobiology Center, NINS, 2-21-1 Osawa, Mitaka, Tokyo 181-8588, Japan

<sup>3</sup>National Astronomical Observatory of Japan, NINS, 2-21-1 Osawa, Mitaka, Tokyo 181-8588, Japan

<sup>4</sup>Department of Astronomy, School of Science, The Graduate University for Advanced Studies (SOKENDAI), 2-21-1 Osawa, Mitaka, Tokyo, Japan

<sup>5</sup>Subaru Telescope, 650 N. Aohoku Place, Hilo, HI 96720, USA

<sup>6</sup>Institute of Engineering, Tokyo University of Agriculture and Technology, 2-24-16, Nakacho, Koganei, Tokyo, 184-8588, Japan

<sup>7</sup>Department of Astronomy, Graduate School of Science, The University of Tokyo, 7-3-1 Hongo, Bunkyo-ku, Tokyo 113-0033, Japan

<sup>8</sup>University of Hawaii, Institute for Astronomy, 640 N. Aohoku Place, Hilo, HI 96720, USA

<sup>9</sup>Faculty of Science and Technology, Oita University, 700 Dannoharu, Oita 870-1192, Japan

<sup>10</sup>Department of Earth Sciences, University of Hawaii at Mānoa, Honolulu, HI 96822, USA

\*E-mail: hirano@geo.titech.ac.jp

Received 2020 May 6; Accepted 2020 August 8

## Abstract

Precision radial velocity (RV) measurements in the near infrared are a powerful tool to detect and characterize exoplanets around low-mass stars or young stars with higher magnetic activity. However, the presence of strong telluric absorption lines and emission lines in the near infrared that significantly vary in time can prevent extraction of RV information from these spectra by classical techniques, which ignore or mask the telluric lines. We present a methodology and pipeline to derive precision RVs from near-infrared spectra using a forward-modeling technique. We applied this to spectra with a wide wavelength coverage ( $Y$ ,  $J$ , and  $H$  bands, simultaneously), taken by the InfraRed Doppler (IRD) spectrograph on the Subaru 8.2-m telescope. Our pipeline extracts the instantaneous instrumental profile of the spectrograph for each spectral segment, based on a reference spectrum of the laser-frequency comb that is injected into the spectrograph simultaneously with the stellar light. These profiles are used to derive the intrinsic stellar template spectrum, which is free from instrumental broadening and telluric features, as well as model and fit individual observed spectra in the RV analysis. Implementing a series of numerical simulations using theoretical spectra that mimic IRD data, we test the

pipeline and show that IRD can achieve  $< 2 \text{ m s}^{-1}$  precision for slowly rotating mid-to-late M dwarfs with a signal-to-noise ratio  $\gtrsim 100$  per pixel at 1000 nm. Dependences of RV precision on various stellar parameters (e.g.,  $T_{\text{eff}}$ ,  $v \sin i$ , [Fe/H]) and the impact of telluric-line blendings on the RV accuracy are discussed through the mock spectra analyses. We also apply the RV-analysis pipeline to the observed spectra of GJ 699 and TRAPPIST-1, demonstrating that the spectrograph and the pipeline are capable of an RV accuracy of  $< 3 \text{ m s}^{-1}$  at least on a time scale of a few months.

**Key words:** methods: data analysis — techniques: radial velocities — techniques: spectroscopic — planets and satellites: detection

## 1 Introduction

M dwarfs are drawing increasing attention in exoplanet studies, for their ubiquity and advantages to search for small planets. The combination of low effective temperatures and small radii of M dwarfs makes the habitable zone (HZ) for exoplanets much closer to their host stars (e.g., Kopparapu et al. 2016), which facilitates the detection and characterization of small planets in the HZ. Recent transit surveys from the space (*Kepler*, *K2*) have unveiled the population of small planets around M dwarfs in unprecedented detail (e.g., Dressing & Charbonneau 2013, 2015; Ballard & Johnson 2016; Gaidos et al. 2016; Dressing et al. 2017), whose properties are similar, but sometimes distinct from those of planets around solar-type stars (e.g., Dressing & Charbonneau 2013; Hirano et al. 2018).

Most previous planet searches around M dwarfs by Doppler observations have been conducted with high-resolution optical spectrographs (e.g., Bonfils et al. 2013; Astudillo-Defru et al. 2017). To take advantage of the characteristic of M dwarfs that they are brighter in the near infrared (NIR), new types of Doppler observations have recently been attempted with NIR high-resolution spectrographs, such as CARMENES at Calar Alto 3.5-m telescope (Quirrenbach et al. 2016), the Habitable-Zone Planet Finder (HPF: Mahadevan et al. 2014) on the Hobby Eberly Telescope, and SPIRou on the CFHT 3.58-m telescope (Artigau et al. 2014a). Some of those NIR instruments are shown to achieve good radial velocity (RV) precisions for M dwarfs similar to those by optical spectrographs<sup>1</sup>.

With a goal of finding small planets in or near the HZ around M dwarfs and characterizing those planets in terms of mass, orbit, and atmosphere, we developed a NIR high-resolution instrument, the InfraRed Doppler (IRD) spectrograph, which was installed on the Subaru 8.2-m telescope in 2017 (Tamura et al. 2012; Kotani et al. 2014, 2018). IRD is a fiber-fed, stabilized spectrograph, which

can simultaneously cover from 930 up to 1740 nm (*Y*, *J*, and *H* bands) with a spectral resolution of  $R \approx 70,000$ . Stellar light collected by the telescope is first focused by the adaptive optics system (AO188: Hayano et al. 2008) and injected into the first fiber through the fiber injection module. A second fiber can be connected to the spectrograph, into which we usually inject the comparison (wavelength calibration) light from the laser-frequency comb (LFC: Kashiwagi et al. 2016; Kokubo et al. 2016). The LFC spectrum consists of a large number of emission lines whose positions are separated by a fixed interval in the frequency domain. The LFC spectrum simultaneously injected with the stellar light is used to correct for any instrumental wavelength (velocity) drift and variations of the point spread function of the spectrograph, which is indispensable for precision and accurate RV measurements by high-resolution spectroscopy.

In this paper, we present our technique and algorithm to derive precision RVs from the NIR spectra, especially acquired by Subaru/IRD. RV measurement techniques have been studied and developed by many groups for a number of spectrographs, most of which exploit cross-correlation based techniques (e.g., Pepe et al. 2002; Bonfils et al. 2013) or forward-modeling ones with the least-squares fitting (e.g., Butler et al. 1996; Sato et al. 2002; Bean et al. 2010; Anglada-Escudé & Butler 2012; Zechmeister et al. 2018). Unlike visible spectra ( $\lambda \lesssim 700 \text{ nm}$ ), however, NIR spectra are heavily contaminated by telluric absorption and emission lines, which can vary in shape due to temporal variations of atmospheric and sky conditions. These variations of telluric lines can lead to large systematic errors in the derived RVs unless taken into account in RV measurements. In the *SERVAL* pipeline (Zechmeister et al. 2018), developed for optical and NIR spectra taken e.g., by CARMENES (Quirrenbach et al. 2016), telluric lines positions are completely masked in the RV fitting procedure. Yet, given that there are very limited ranges of the spectrum (e.g.,  $990 \text{ nm} < \lambda < 1070 \text{ nm}$ ) that are nearly free from telluric absorptions in the whole wavelength region covered

\* Based on data collected at Subaru Telescope, which is operated by the National Astronomical Observatory of Japan.

<sup>1</sup> See e.g., <https://hpf.psu.edu>

by IRD ( $970\text{nm} < \lambda < 1720\text{nm}$ ), this masking scheme for all the telluric lines does not work for the RV analyses of IRD spectra. This difficulty in handling the telluric lines in the NIR, as well as the instrumental characteristics of IRD (e.g., the use of the LFC for a simultaneous reference), made us develop our own pipeline to derive RVs from NIR spectra by the forward-modeling technique in the presence of time-variable telluric lines.

The rest of this paper is organized as below. In Section 2, we briefly describe the observations of several standard stars using Subaru/IRD and present the data reduction to extract one-dimensional (1D) spectra. Section 3 presents the detailed descriptions on our scheme and methodology to derive precision RVs from the IRD spectra. We first test the RV pipeline using theoretical (mock) spectra which are generated based on the properties of the IRD spectrograph and theoretically synthesized M-dwarf spectra (Section 4). In the same section, we discuss the RV precisions achievable for different types of stars (e.g., spectral type, rotation velocity, stellar metallicity, etc) through a series of Monte Carlo simulations. To demonstrate the on-sky performances of IRD, we analyze the data of GJ 699 and TRAPPIST-1 using our pipeline, and Section 5 summarizes the results. Section 6 is devoted to the summary and discussion, in which we also present the future prospects to improve the pipeline.

## 2 Observations and Data Reduction

We carried out observations of several standard stars (RV and telluric standards) with Subaru/IRD during IRD’s engineering nights in 2018 and open-use programs in 2018 and 2019 to test and demonstrate IRD’s on-sky performances. Targets of observations are explained in more detail in Section 5. For each observing run (typically a few to 10 nights), we took flat-lamp frames for each of the two fibers. For the comparison spectra, we used both Thorium-Argon (Th-Ar) hollow cathode lamp and LFC.

Raw IRD frames were reduced by the standard procedure for echelle data reductions. Since the HAWAII-2RG detectors used in IRD are known to show count biases that are dependent on each readout channel, we used our custom code to suppress the bias counts (Kuzuhara et al. 2018). The subsequent reduction steps (flat fielding, scattered light subtraction, extraction of one-dimensional spectra, and wavelength calibration with the Th-Ar lamp) were performed using the echelle package of IRAF. Approximate wavelength calibration was done based on emission lines of the Th-Ar comparison spectrum (Kerber et al. 2008), which covers the whole range of IRD spectra. For precise RV measurements, however, both the precision and accu-

racy of the wavelength calibration are not good enough to achieve  $\approx 1\text{ m s}^{-1}$  due to the lack of strong Th-Ar lines in the NIR, and thus we recalibrated the wavelengths using the LFC spectrum for each fiber. For the recalibration of wavelength, we fitted individual emission lines of LFC by Gaussians and identified peak positions for all available lines. We then reassigned the wavelength to each pixel so that the peak positions are exactly separated by 12.5 GHz in the frequency domain (= designed separation of LFC emission lines  $\approx 0.042\text{ nm}$  at 1000 nm). LFC spectrum currently covers between 1050 nm and 1720 nm (Figure 1), thus we were capable of this recalibration for only those wavelengths. Below 1050 nm, we kept the wavelength solutions determined by the Th-Ar lamp and we did not use those shorter wavelengths for RV measurements in Section 5.

## 3 Methodology

In this section, we briefly introduce the concept of RV measurements using simultaneous observations of a reference spectrum and illustrate the characteristics of the IRD spectrograph, with which we reach the conclusion that we need forward modeling to derive accurate RVs from IRD spectra. Our RV analysis pipeline is described in detail in subsection 3.3.

### 3.1 Simultaneous Reference Technique

In the simultaneous reference technique, precision stellar RVs are usually measured in two steps. First, using the wavelength-calibrated 1D stellar spectrum, absolute RVs from the positions of absorption lines are measured. This is often done by cross-correlating the observed spectrum against a template spectrum; the most successful optical spectrographs (e.g., ESO/HARPS) adopt box-shaped numerical masks as template spectra (e.g., Pepe et al. 2002). Let us denote this measured RV by  $v_{\text{obs}}$ . The second step is the measurement of the “drift” of the spectrum due to environmental variations of the spectrograph (i.e., temperature and pressure). The spectral drift of order  $10^{-3}$  pixel usually translates to an apparent RV variation of  $1 - 2\text{ m s}^{-1}$ ; the correction of this small pixel drift is essential to achieve extreme precisions. In order to assess the spectral drift, the wavelength-reference spectrum (e.g., from a Th-Ar lamp) is obtained simultaneously and cross-correlated against a template wavelength-reference spectrum. Under the assumption that the pixel (or velocity) drift of the stellar spectrum is exactly the same as that of the reference spectrum, the RV drift  $v_{\text{drf}}$  is estimated by fitting the cross-correlation function (CCF) by e.g., a single Gaussian

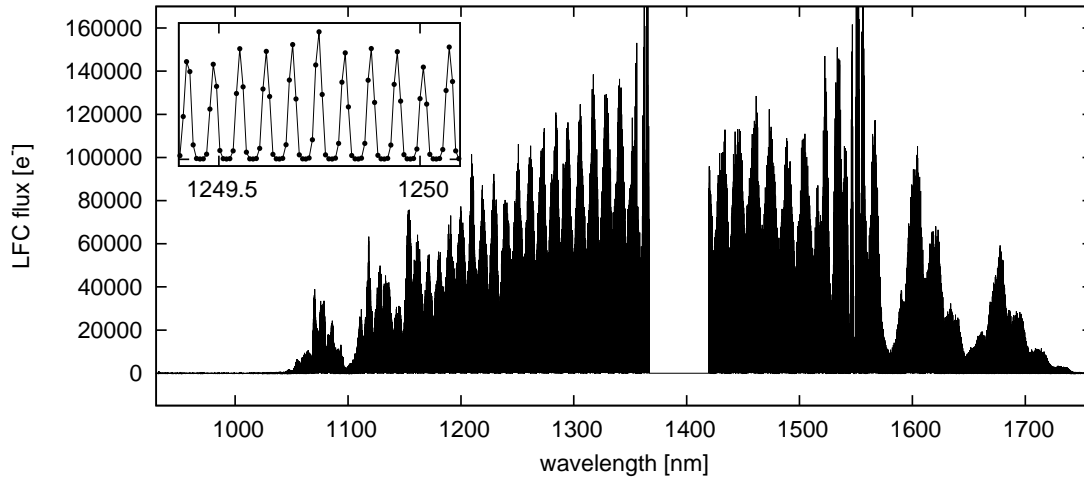


**Fig. 1.** A sample of LFC spectrum taken by Subaru/IRD with the integration time of 300 sec. Each mountain-shaped feature (periodic) corresponds and reflects the blaze function of each echelle order. The inset displays a small region of the same spectrum ( $1249.4 \text{ nm} < \lambda < 1250.1 \text{ nm}$ ).

and measuring the center of the CC function. The final stellar RV  $v_*$  is then determined by

$$v_* = v_{\text{obs}} - v_{\text{drift}}. \quad (1)$$

For IRD, the LFC, injected into the reference fiber, is designed to correct for the instrumental drifts by precise tracking of the LFC line positions. See Figure 1 for a sample LFC spectrum taken with a 5-minute integration.

Since it is essential to set the offset between the wavelength solutions for both fibers to zero, for the absolute wavelength calibration we split the calibration-source (either Th-Ar lamp or LFC) light into the two fibers and inject those into the IRD spectrograph simultaneously; if those calibration sources are not observed simultaneously for the two fibers, the temporal drift of spectrum positions leads to a systematic relative offset between the two wavelength solutions for the two fibers. This offsetting needs to be done for each IRD observing run, as the position of the IRD echellogram is also known to move along the “spatial” direction on the detectors over a time scale of a few months to a year, due to variations in environmental conditions (Kotani et al. in prep.). Every time a new set of calibration data with the LFC (or Th-Ar) being injected into both fibers is obtained, wavelengths are calibrated based on the procedure described in Section 2 for each fiber.

### 3.2 Instrumental RV Drift of IRD

IRD exhibits temperature variations, typically a few 10 mK to over 100 mK (peak-to-valley), depending on the position of the measurement point. This temperature variation, probably arising from electrical drift of the temperature sensors and/or temperature controller, was found to

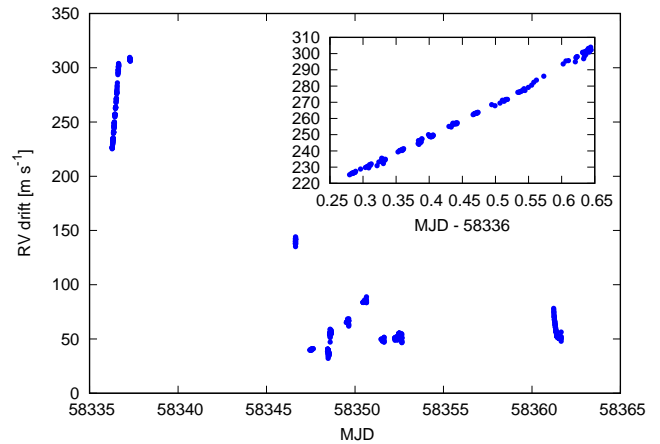


**Fig. 2.** RV drift (representative value for all spectral segments) of the IRD spectrograph during a month. The RV variation within a night is plotted in the inset.

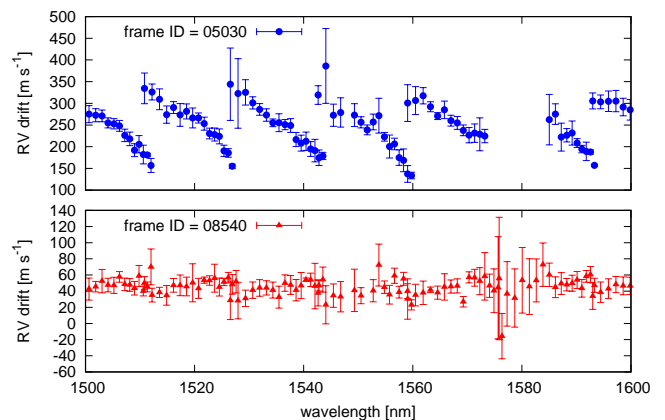


**Fig. 3.** RV drifts measured at individual spectral segments (each  $\Delta\lambda = 0.7 - 1 \text{ nm}$ ) for two different frames taken in 2018 August.

cause a large apparent RV drift in time. Figure 2 plots the observed RV drift of IRD, measured using the LFC spectra taken during 2018 August; We computed the RV drift of each LFC spectrum by cross-correlating it against a template LFC spectrum, which is generated by combining a large number ( $> 50$ ) of LFC frames taken during a relatively short time interval. As shown in the figure, the RV drift could be as large as  $\approx 300 \text{ m s}^{-1}$ , and RVs can vary by  $> 50 \text{ m s}^{-1}$  even during a single night. Similar RV drifts measured from LFC data were also reported in Kuzuhara et al. (2018). We found that the RV drift of the spectrograph is strongly correlated with temperature variations of the camera lens just in front of the detectors (Kotani et al. in prep.).

In addition to this overall RV drift (i.e., averaged over all orders) in time, the apparent RV drift of the LFC spectrum depends on the position on the detector; when we split the whole spectrum into many small spectral segments (e.g.,  $\approx 1 \text{ nm}$ ), each spectral segment was found to have a different RV drift value, which is more evident when the overall (mean) RV drift is large. Figure 3 displays the results of segment-by-segment drift measurements for two different IRD frames. In this figure, we split each echelle order into 19 segments and fitted each segment with LFC emission lines to the template LFC spectrum by the least-squares technique. The positional dependence of the RV drift is more significant when the overall RV drift is large (ID = 05030; upper panel), while the RV drift takes similar values for all segments (different orders) when the overall RV is relatively small (ID = 08540; lower panel). The primary reason for this positional dependence is that each pixel on the IRD detectors does not cover the same interval in wavelength nor velocity, and the parallel pixel shift of the spectrum results in a different degree of drift in the velocity. For example, for the echelle order of 95, one pixel covers  $\Delta\lambda \approx 0.0055 \text{ nm}$  at the shortest-wavelength edge of the order, but it corresponds to  $\Delta\lambda \approx 0.0135 \text{ nm}$  at the other edge of the detector. This implies that a pixel shift of e.g., 0.1 pixel corresponds to the velocity drifts of  $\approx 110 \text{ m s}^{-1}$  at the shortest-wavelength edge and  $\approx 260 \text{ m s}^{-1}$  at the longest-wavelength edge of the same order, respectively. This fact qualitatively explains the behaviors in Figure 3 at least as an approximation<sup>2</sup>. The fact that the wavelength (velocity) coverage is different for each pixel on the detector suggests that a temperature instability of the spectrograph leads not only to a parallel shift of the spectrum against wavelength or velocity, but also to an effective width (shape) variation of the “instrumental profile” (IP) in the velocity domain for each spectral segment; therefore Equation (1) cannot be used to correct for the

<sup>2</sup> More precise effects of the spectrum shift are under investigation.

instrumental drift for the case of IRD.

### 3.3 RV Analysis Pipeline of IRD

Besides the instrumental challenges above, strong telluric spectral features are a major issue for NIR RV measurements. The telluric imprints can significantly vary depending on the target’s airmass and observing conditions (humidity, in particular). In NIR spectroscopy, standard stars have been traditionally observed immediately before and/or after the scientific exposures to correct for the telluric lines, but it is unrealistic in a Doppler survey to point to standard stars for every exposure of a target.

Based on all these technical challenges and characteristics of the IRD instrument, we decided to adopt a forward-modeling technique in the RV analysis for IRD data. RV measurements at visible wavelengths using forward-modeling techniques have been discussed in the literature, especially for measurements with the iodine absorption cell (e.g., Butler et al. 1996; Sato et al. 2002). Figure 4 shows the flow chart of the IRD data reduction and RV measurements. Instead of employing the classical CCF technique often used in the optical simultaneous-reference technique, we attempt to correct for the impacts of time-variable telluric lines and IPs by modeling an observed NIR spectrum  $f_{\text{obs}}(\lambda)$  as

$$f_{\text{obs}}(\lambda) = k(\lambda) \times \left[ S \left( \lambda \sqrt{\frac{1+v_*/c}{1-v_*/c}} \right) T \left( \mathbf{A}; \lambda \sqrt{\frac{1+v_{\text{tel}}/c}{1-v_{\text{tel}}/c}} \right) \right] * \text{IP}, \quad (2)$$

where  $*$  represents the convolution operator, and  $S(\lambda)$  is the intrinsic stellar spectrum (free of telluric lines), Doppler-shifted by the stellar RV  $v_*$ . The telluric absorption spectrum  $T(\mathbf{A}; \lambda)$  includes a few relevant telluric parameters  $\mathbf{A}$  (i.e., precipitable water vapor amount, target airmass). The telluric velocity-shift  $v_{\text{tel}}$  is introduced so as to take into account a possible small variation of telluric line positions, due to e.g., winds. The factor  $k(\lambda)$  represents the overall normalization of the spectral continuum, which we express by a quadratic function of wavelength  $\lambda$ . IP denotes the instrumental profile of the spectrograph, whose shape depends on wavelength (= position on the detector).

One advantage of the forward-modeling RV measurement by Equation (2) is that since the exact wavelength positions of all LFC lines are known *a priori*, any relative instrumental RV drifts as well as variations in the spectrograph’s point-spread function can be precisely traced by extracting the instantaneous IP from the LFC spectrum; the extracted IP for each spectral segment should contain those pieces of information, and the overall velocity shift

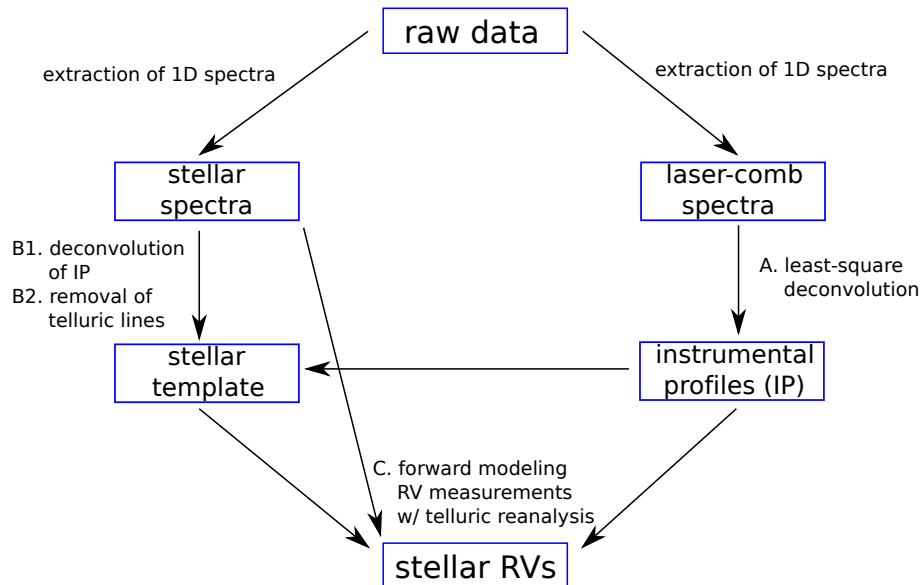


Fig. 4. Flowchart of the RV analysis pipeline for Subaru/IRD.

of the extracted IP’s centroid corresponds to the instrumental RV drift of that segment. Hence, by convolving this extracted IP in modeling an observed stellar spectrum (Equation (2)), one no longer needs to subtract segment-by-segment instrumental drifts as in Equation (1). In this methodology, it is important to use “fixed” wavelength solutions for all frames<sup>3</sup> obtained during a run (Section 2), since IP extraction from the LFC spectrum traces “relative” variations in time.

We split the observed spectrum of each echelle order into 19 small spectral segments, each spanning a wavelength range of  $\Delta\lambda = 0.7 - 1$  nm, and the RV fitting is performed for each segment (step “C.” in Figure 4). Equation (2) is somewhat similar to the expression for the forward-modeling RV measurements in the visible using the iodine cell (e.g., Equation (1) of Sato et al. 2002). Also in the NIR, Bean et al. (2010) developed a forward-modeling technique, similar to our method, for RV measurements with the “ammonia” cell from  $K$ -band spectra. Unlike those forward-modeling techniques, however, IPs in our RV analysis (Equation (2)) are independently determined based on the reference (LFC) spectrum. Note that time-variable telluric lines are simultaneously modeled in our RV fit, which are usually ignored in the optical RV analysis. Below, we describe how we extract (generate) each component that appears in Equation (2), and the procedure to compute the RV value for each IRD frame.

### 3.3.1 Extraction of the IP for Each Segment

Estimation of the instantaneous IP for each frame, for each spectral segment, is the essential part of the forward-modeling technique for precision RV measurements. In the pipelines of optical RV measurements using the iodine cell, instantaneous IPs are estimated from the shapes of the iodine absorption lines, which are blended with stellar spectrum (e.g., Butler et al. 1996; Sato et al. 2002). In most cases, the IPs are modeled by a linear combination of multiple Gaussian functions, whose heights are optimized simultaneously in fitting the stellar RV. For the case of the simultaneous reference method using LFC, the shapes of LFC emission lines directly reflect the instantaneous IP for each spectral segment, and we can determine the IP shape separately from the stellar RV measurement.

Since the intrinsic width of LFC emission lines ( $\sim 1$  MHz =  $1 - 2$  m s<sup>-1</sup> in the velocity domain) is three orders of magnitude smaller than the spectral resolution of IRD ( $\approx 4$  km s<sup>-1</sup>), an intrinsic LFC spectrum is well approximated by a combination of the Dirac delta functions, separated by a fixed interval (12.5 GHz) in the frequency domain (i.e., what we observe in the LFC spectrum is almost equivalent to the IP of the spectrograph). In this case, we can use the least square deconvolution (LSD) technique to extract the “mean” line profile for each spectral segment. In the standard LSD (e.g., Donati et al. 1997), the observed flux vector  $\mathbf{Y}$  of the LFC spectrum is expressed by a product of the emission-line matrix  $M$  and IP vector:

$$\mathbf{Y} = M\mathbf{IP}. \quad (3)$$

The matrix elements of  $M$  are given by Equations (17) and (18) in Donati et al. (1997). For a given  $M$ , the least-

<sup>3</sup> Note that wavelength solutions are different for LFC and stellar fibers.

squares solution for the IP vector is computed by

$$\text{IP} = (M^T S^2 M)^{-1} M^T S^2 \mathbf{Y}, \quad (4)$$

where

$$S^2 = \text{diag} \left( \frac{1}{\sigma^2} \right) \quad (5)$$

is the vector containing the reciprocal flux errors ( $\{1/\sigma_i\}$ ). This IP extraction is easy to execute, but the IP estimation based on this standard LSD is known to have the “noise amplification” problem especially when the input spectrum has a relatively large noise, or the pixel sampling of the input spectrum is sparse, due to the nature of direct “deconvolution” processes (Donati et al. 1997). For the case of IRD’s LFC, each LFC line is sampled with only 4–5 points (Figure 1), which are much sparser than the velocity resolution we want for the extracted IP ( $\lesssim 0.5 \text{ km s}^{-1}$ ).

Fortunately, we know that IP is generally a “smooth” function in the velocity (or wavelength) domain since it originates from the spectrograph’s point spread function on the detector. To take into account this *a priori* information, we estimate the IP by the Bayesian inference technique, following the formulation by Asensio Ramos & Petit (2015); they model the pixel-to-pixel correlations in the LSD profile by a Gaussian process regression (e.g., Gibson et al. 2012; Evans et al. 2015):

$$p(\text{IP}|\boldsymbol{\alpha}) = \mathcal{N}(\text{IP}|\mathbf{0}, K(\boldsymbol{\alpha})), \quad (6)$$

where  $\mathcal{N}$  represents a multivariate Gaussian function and  $K(\boldsymbol{\alpha})$  is the covariant matrix determining the pixel-to-pixel correlations in the IP, which is characterized by  $\boldsymbol{\alpha}$  (a vector whose dimension corresponds to the number of hyperparameters). Here, we adopt the squared exponential kernel for the covariant matrix whose components are expressed as

$$K_{ij} = K^2 \exp \left\{ -\frac{(v_i - v_j)^2}{2L^2} \right\}, \quad (7)$$

where  $v_i$  represents  $i$ -th velocity component of the IP function, and  $K$  and  $L$  are hyperparameters that determine the amplitude and length of correlations in the profile. In this formulation,  $\boldsymbol{\alpha} = (K, L)$ . Equation (7) includes no uncorrelated (white) noise term, since we require a smooth functional dependence for the IP.

What we want to learn now is the posterior distribution of IP conditioning on the observed LFC spectrum  $\mathbf{Y}$ , but this probability distribution  $p(\text{IP}|\mathbf{Y})$  in general cannot be derived analytically. A solution to this is to adopt an approximation called Type-II maximum likelihood, in which  $p(\text{IP}|\mathbf{Y})$  is approximated as

$$p(\text{IP}|\mathbf{Y}) \propto \int p(\mathbf{Y}|\text{IP})p(\boldsymbol{\alpha})p(\text{IP}|\boldsymbol{\alpha})d\boldsymbol{\alpha}$$

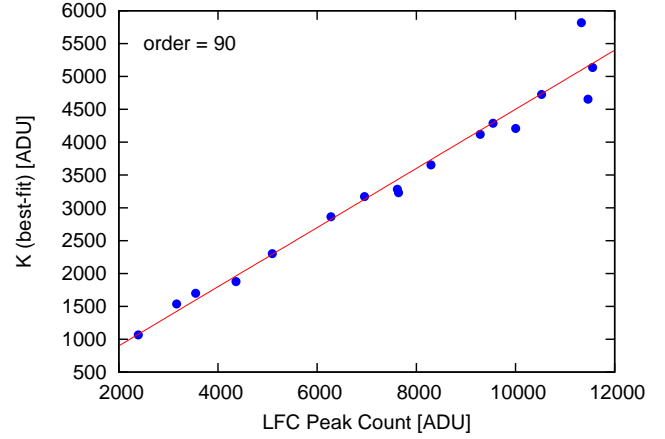


Fig. 5. Optimized hyperparameter  $K$  (correlation amplitude) for each spectral segment as a function of LFC’s peak count within the same segment.

$$\approx p(\mathbf{Y}|\text{IP})p(\text{IP}|\hat{\boldsymbol{\alpha}}), \quad (8)$$

where  $\hat{\boldsymbol{\alpha}}$  represents the set of hyperparameters that maximizes the posterior probability of  $\boldsymbol{\alpha}$  conditioning on the data  $p(\boldsymbol{\alpha}|\mathbf{Y})$  (Asensio Ramos & Petit 2015). Since  $p(\mathbf{Y}|\text{IP})$  is the standard likelihood

$$p(\mathbf{Y}|\text{IP}) = \mathcal{N}(\mathbf{Y}|M\text{IP}, S^{-2}), \quad (9)$$

Equation (8) reduces to

$$\begin{aligned} p(\text{IP}|\mathbf{Y}) &\approx \mathcal{N}(\mathbf{Y}|M\text{IP}, S^{-2})\mathcal{N}(\text{IP}|\mathbf{0}, K(\hat{\boldsymbol{\alpha}})) \\ &= \mathcal{N}(\text{IP}|\boldsymbol{\mu}, \Sigma), \end{aligned} \quad (10)$$

where

$$\Sigma = [K(\hat{\boldsymbol{\alpha}})^{-1} + M^T S^2 M]^{-1} \quad (11)$$

$$\boldsymbol{\mu} = \Sigma M^T S^2 \mathbf{Y}. \quad (12)$$

Equation (12) gives the mean function of the IP based on the Bayesian LSD. In the absence of pixel-to-pixel correlations ( $K(\boldsymbol{\alpha}) = 0$ ), this expression is equivalent to the standard LSD solution (Equation 4).

The posterior probability  $p(\boldsymbol{\alpha}|\mathbf{Y})$  is computed as

$$\begin{aligned} p(\boldsymbol{\alpha}|\mathbf{Y}) &\propto \int p(\mathbf{Y}|\text{IP})p(\text{IP}|\boldsymbol{\alpha})p(\boldsymbol{\alpha})d\text{IP} \\ &= p(\boldsymbol{\alpha})\mathcal{N}(\mathbf{Y}|\mathbf{0}, \Sigma_{\boldsymbol{\alpha}}), \end{aligned} \quad (13)$$

where

$$\Sigma_{\boldsymbol{\alpha}} = S^2 + MK(\boldsymbol{\alpha})M^T, \quad (14)$$

and  $p(\boldsymbol{\alpha})$  is the prior distribution for  $\boldsymbol{\alpha}$ . In case that no prior is imposed on  $\boldsymbol{\alpha}$ ,  $\hat{\boldsymbol{\alpha}}$  that gives the maximum posterior probability (13) is estimated by minimizing the following  $\chi^2$  statistics:

$$\chi^2 = \mathbf{Y}^T \Sigma_{\boldsymbol{\alpha}}^{-1} \mathbf{Y} + \log |\Sigma_{\boldsymbol{\alpha}}|, \quad (15)$$

where  $|\Sigma_{\boldsymbol{\alpha}}|$  is the determinant of  $\Sigma_{\boldsymbol{\alpha}}$ .

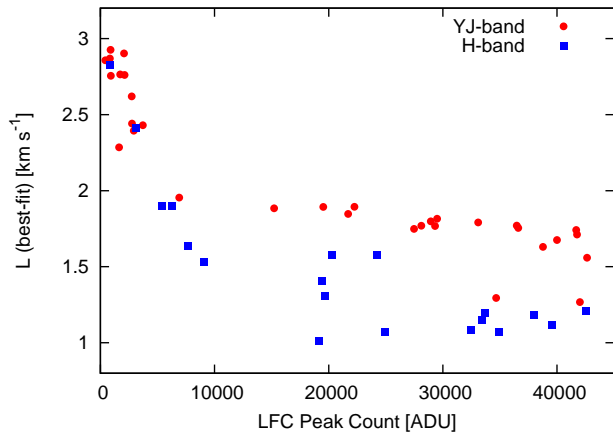


Fig. 6. Optimized hyperparameter  $L$  (correlation length in the velocity domain) as a function of LFC’s median peak count for each order.

We apply this Bayesian LSD to LFC spectra and extract instantaneous IPs for individual frames. As we stated in Section 3.2, IPs of the IRD spectrograph are different from order to order, and from segment to segment. Therefore, we split each echelle order of a whole LFC spectrum into 19 segments, each spanning 100 – 110 pixels ( $\Delta\lambda = 0.7 - 1$  nm), and computed Equation (12) for each segment. This number of segments for each order was empirically determined taking into account (1) the number of available LFC emission lines, (2) similarity/difference in the IPs of adjacent segments, and (3) CPU time to compute the inverse matrix in the LSD. Spectral segments corresponding to both edges of each order are excluded from the analysis, since significant fractions of pixels for those segments have near-zero flux counts due to vignetting on the detector.

Ideally, one should optimize the hyperparameter  $\alpha$  for each frame, for each spectral segment, by minimizing Equation (15). However, the equation involves an inverse matrix calculation, which is computationally expensive. In the real data analysis, therefore, we decided to take an approach to fix the hyperparameters in computing Equation (12) to empirical values pre-determined by our analysis of typical LFC spectra; the implicit assumption in this empirical approach is that the hyperparameters that give the best description of observed LFC spectra do not significantly vary for each frame, but depend only on the peak counts and wavelengths of LFC emission lines.

Allowing the two hyperparameters in Equation (7) to float freely, we performed the minimization of Equation (15) for a set of typical LFC spectra using the Nelder-Mead simplex method (e.g., Press et al. 2002). Figure 5 plots an example of the optimized hyperparameter  $K$  for 17 segments of one specific echelle order. The horizontal axis of the figure is the mean peak count of LFC emission lines within the same segment. As is evident from the fig-

ure,  $K$  giving the minimum  $\chi^2$  is almost proportional to the mean peak of the LFC lines. The red solid line in the same figure indicates the result of a linear regression to the 17 points (slope  $\approx 0.45$ ). We also checked for the variation of the optimal  $L$  (the correlation scale in the velocity domain) for many different segments, finding that the optimal  $L$  is also dependent on the typical LFC intensity (i.e., S/N ratio) for individual orders. The optimal  $L$  averaged within each order is plotted in Figure 6 as a function of the median LFC peak count of that order; A higher value of  $L$  is preferred for orders with lower LFC intensities, while the quantitative behaviors are slightly different for YJ-band and H-band detectors. The velocity scale covered by each pixel of the detector differs significantly from order to order (and from segment to segment), but this general trend implies that the optimal correlation length is grossly affected by the S/N ratio of the LFC lines, and a longer correlation length is generally required to smooth out noisier spectra. From those analyses, we derived the empirical values for the two hyperparameters for each order, and those parameters are held fixed at those values in the subsequent analyses.

Figure 7 plots instances of the IPs estimated using Equation (12) for an observed LFC spectrum, taken on UT 2018 August 6. The three panels show the three different segments’ IPs for echelle order = 125 ( $1171 \text{ nm} < \lambda < 1185 \text{ nm}$ ), order = 91 ( $1608 \text{ nm} < \lambda < 1629 \text{ nm}$ ), and order = 90 ( $1626 \text{ nm} < \lambda < 1647 \text{ nm}$ ), respectively. As expected, the IP shape in the velocity domain is heavily dependent on the position of the detector and each IP is not symmetric with respect to the line center. Moreover, the IP variation within one order is not always monotonic against wavelength; the IP is the sharpest around the central part (segment = 10) of the 125th spectral order, while they are similar in shape in both edges (segment = 5 and 15) of the spectrum for that order. On the other hand, IP has the highest peak at longer wavelengths for order = 90 and order = 91. IPs of the same segment number in the neighboring orders are similar in shape, as shown in Figure 7.

IPs are well extracted only when the S/N ratio of the spectral segment is sufficiently high enough, but it is not straightforward to estimate IPs for segments with low S/N ratios. In particular, when a LFC spectrum is taken with relatively short integration time ( $< 1$  minute), the detector’s readout noise is more significant in comparison with LFC emissions in some orders (cf. Kuzuhara et al. 2018). In addition, as a characteristic of IRD’s LFC, emission lines are not generated with good S/N ratios at certain wavelengths (e.g., around 1100 nm and 1550 nm; see Figure 1). For those segments, we estimate the IPs by interpo-

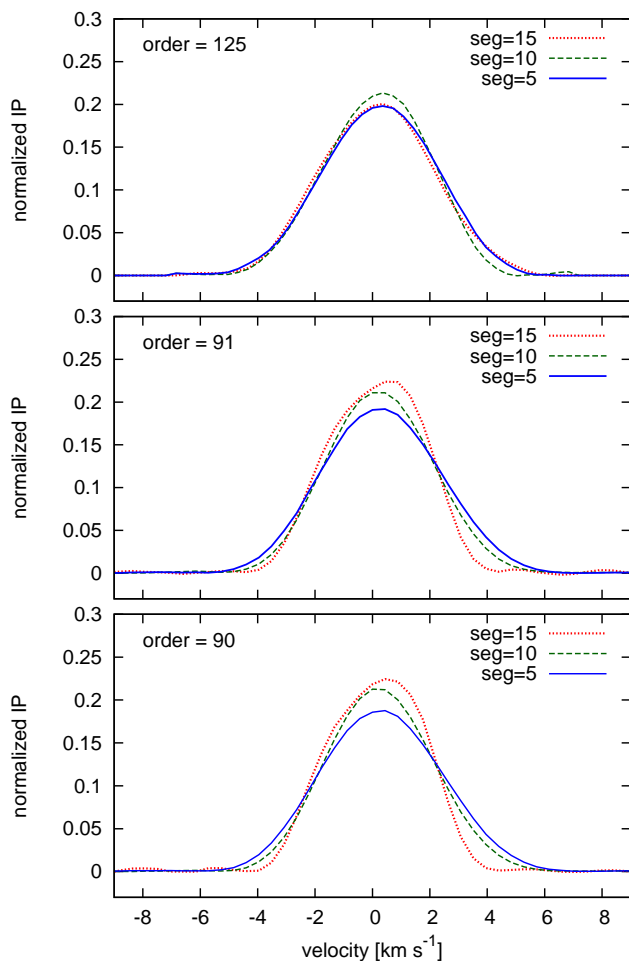


Fig. 7. Extracted IPs for three different spectral segments of echelle order 125 (top), 91 (middle), and 90 (bottom).

lating the IPs of segments that are neighboring, for which IPs are properly extracted from the LFC emission lines. The interpolation does not only use the adjacent (or near) segments within the same order, but also refers the IPs of similar segment numbers in the neighboring orders, on the assumption that the point spread function of the spectrograph “gradually” varies in both spatial and wavelength directions on the detector. The similarity of IPs in the neighboring orders shown in Figure 7 reinforces this statement. Since the current LFC covers wavelengths between 1050 nm and 1730 nm, we can only extract IPs for the segments beyond 1050 nm. Below 1050 nm, we adopt the mean IPs over the *Y*-band spectrum, but those segments below 1050 nm are not used in the RV analysis for observed spectra (Section 5).

### 3.3.2 Telluric Absorption Spectrum $T(\mathbf{A}; \lambda)$

For the telluric transmittance  $T(\mathbf{A}; \lambda)$ , we use the theoretical transmission spectra generated by Line By Line

Radiative Transfer Model (LBLRTM; Clough et al. 2005). To save the computation time in fitting the spectrum, we synthesized the telluric transmittance at  $4 \times 4$  grid points for the precipitable water vapor content ( $W$ ) and target’s airmass ( $A$ ), covering realistic ranges of those parameters ( $1.0\text{mm} < W < 5.0\text{mm}$  and  $1.0 < A < 2.9$ ). For each grid point in the  $\mathbf{A} = (W, A)$  plane, we generated a telluric spectrum for the atmosphere above the summit of Maunakea. In doing so, the  $T - p$  (and height  $H$ ) profile and volume mixing ratio of each atmospheric molecule are required. Following Rudolf et al. (2016), we employed the averaged profiles based on the Global Data Assimilation System (GDAS)<sup>4</sup> sounding files at the location of Maunakea for  $H \leq 26$  km, and also downloaded the MIPAS<sup>5</sup> mid-latitude night-time profiles for  $H > 26$  km. We then input these profiles into the LBLRTM code, which generates the telluric transmission spectrum in the NIR with the input variables, ( $W, A$ ). In the RV fit (Equation 2), the telluric spectrum  $T(\mathbf{A}; \lambda)$  is generated by interpolation of those template telluric spectra on the ( $W, A$ ) grid, and  $\mathbf{A}$  is optimized simultaneously.

In the NIR, some spectral segments are also contaminated by night-glow emission lines, which are particularly prominent in the *H*-band data. In the RV analysis, we simply mask all those emission lines based on the theoretical radiance model generated by SkyCalc (Noll et al. 2012; Jones et al. 2013), by which the number of usable pixels for spectrum fitting is reduced by only 1 – 2% for most echelle orders.

### 3.3.3 Estimation of the Intrinsic Stellar Spectrum $S(\lambda)$ (Template for RV Fits)

One tricky part of the forward-modeling technique for RV measurements in the NIR is the estimation of the intrinsic stellar spectrum  $S(\lambda)$ . In the NIR, stellar spectra are heavily contaminated by the telluric absorptions and nightglow emissions, which complicates the extraction of a telluric-free stellar template. Moreover, the molecular line lists are often incomplete or inaccurate (e.g., Tennyson & Yurchenko 2018), and thus theoretically synthesized spectra disagree with observed ones, meaning that we cannot use those model spectra as templates for RV measurements by the forward-modeling technique.

Fortunately though, stellar line positions are not constant in time due to the barycentric motion of Earth, while telluric line positions are almost unchanged against wavelength, which helps us disentangle the stellar lines from telluric ones. To extract the stellar template, the first step

<sup>4</sup> <https://ready.arl.noaa.gov/READYcmet.php>

<sup>5</sup> The Michelson Interferometer for Passive Atmospheric Sounding (MIPAS) model atmosphere: <http://www-atm.physics.ox.ac.uk/>

is deconvolution of the instantaneous IP for each spectral segment (step “B1.” in Figure 4). This is carried out by using the IP estimated from the LFC spectrum for the same spectral segment. For IP deconvolutions, we use the “iterative/recursive” deconvolution described in Coggins et al. (1994) and Sato et al. (2002), in which, unlike LSD, one does not need to assume the intrinsic profile is expressed by the delta function.

The second step is to remove the telluric absorption lines from the IP-deconvolved spectrum (step “B2.” in Figure 4) using theoretically synthesized telluric spectra as in Section 3.3.2. We apply the least-squares technique to each echelle order of an observed spectrum in order to model the telluric transmittance and estimate the best-fit telluric parameters ( $\mathbf{A}$  and  $v_{\text{tel}}$ ), together with the continuum polynomial. Since intrinsic stellar lines are not known at this point and they are blended with telluric features in each observed spectrum, fitting the telluric lines by theoretical models is affected by the contaminating stellar lines. To mitigate this impact, we empirically imposed more “weights” on pixels corresponding to deeper telluric lines so that spectral parts having no (or very shallow) telluric features have minimal contributions to the spectrum fitting.

We developed another option to remove telluric absorptions to create an intrinsic stellar spectrum  $S(\lambda)$ . This is based on the telluric standard star (rapid rotator having a featureless spectrum) immediately observed before or after an RV target. By dividing the target spectrum by a normalized spectrum of the telluric standard, we can remove telluric absorption lines, unless they are saturated (i.e., near zero flux counts). Note that these observed telluric spectra are used only for the construction of the stellar template, and not each time for an RV measurement. For this option, we deconvolve the IP from the telluric-removed stellar spectrum to obtain the intrinsic stellar template. This operation is not mathematically equivalent to the procedure for real data acquisition; multiplication of the telluric transmittance and convolution of IP are not mathematically commutative. However, our experience with the observed data suggested the deconvolution “after” the telluric removal yields a good approximation to the intrinsic stellar template. This procedure also does not remove the nightglow emission lines.

Each IP-deconvolved, telluric-removed stellar spectrum derived by the above steps is cross-correlated against a theoretical stellar template (PHOENIX BT-SETTL: Allard et al. 2013) to roughly estimate the stellar RV for that frame, and the spectrum is Doppler-shifted by the RV such that the resulting spectrum is in the stellar rest frame. The theoretical template for cross-correlations should ideally be

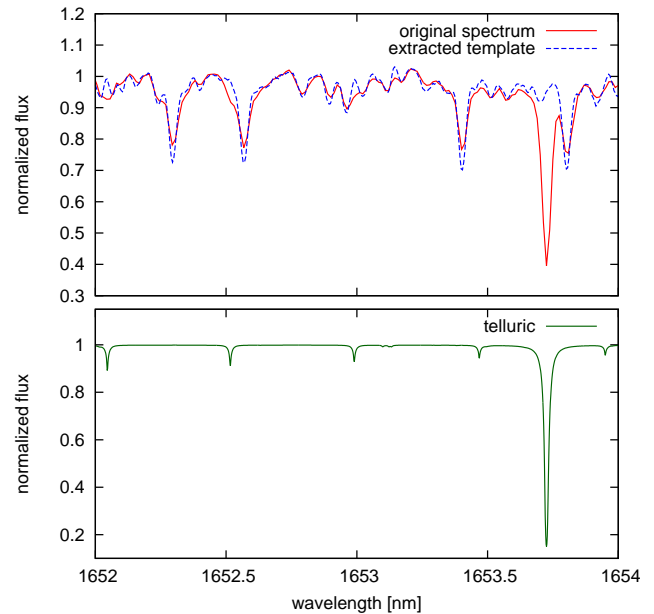


**Fig. 8.** (*Upper*) Observed spectrum (before any processing; red solid line) v.s. IP-deconvolved, telluric-removed template (blue dashed line) for GJ 699. (*Lower*) Theoretical telluric transmittance in the same region, before the convolution of the IP.

generated based on the accurate stellar parameters of the target star (e.g.,  $T_{\text{eff}}$ ,  $\log g$ ,  $[\text{Fe}/\text{H}]$ ), but our experience has shown that a small difference in those parameters has a negligible impact on the rough RV estimation. We thus prepared only two theoretical templates for RV measurements of our target stars presented in this paper as well as other M-dwarf targets during the engineering observations ( $T_{\text{eff}} = 2700, 3100$  K,  $\log g = 5.0$ ,  $[\text{Fe}/\text{H}] = 0.0$ ). Since deconvolution is known to increase the flux noise and telluric removal by the above steps cannot completely clean off telluric lines as well as nightglow emissions for individual frames, we median-combine multiple frames ( $> 10$  preferred) to gain a high S/N stellar template, free of telluric lines. In doing so, it is important to obtain spectra of the same target star on well separated nights; the stellar lines can be Doppler-shifted by Earth’s barycentric motions by up to  $\approx \pm 30$  km s $^{-1}$  (except targets at high ecliptic latitudes). Thus, acquisitions of multiple-epoch spectra whose barycentric RV corrections are separated by  $\gtrsim 4$  km s $^{-1}$  (= resolution of IRD) enable us to well distinguish stellar line positions from the telluric ones.

Figure 8 depicts a comparison between an observed IRD spectrum of GJ 699 and the extracted template for the same target based on the above procedure. Both spectra are normalized and Doppler-shifted to the same reference. More than 20 frames are combined to obtain this template. As is evident in the figure, stellar lines become sharper by deconvolution of IP. The strong line at  $\approx 1653.7$  nm is

telluric absorption, which was completely removed in the output stellar template.

We applied our pipeline to extract intrinsic stellar templates for various stars observed by IRD. Figure 9 illustrates three examples of extracted stellar templates (deconvolved and telluric-removed): an early-M dwarf (GJ 436: top), a mid-M dwarf (GJ 699: middle), and a late-M dwarf (TRAPPIST-1: bottom). The two gaps at 1110–1150 nm and 1330–1495 nm correspond to the strong telluric regions and the gap between 2 detectors, respectively, for which we are unable to extract clean templates. Figure 9 indicates that the later-type stars have deeper and denser features of molecular lines, which leads to higher RV information content for those targets.

### 3.3.4 RV Fitting for Individual Segments

Using all the components generated by the above steps, we fit the observed spectrum  $f_{\text{obs}}(\lambda)$  by Equation (2) for each spectral segment spanning  $\approx 1$  nm. The basic fitting parameters here are the three coefficients of the polynomial  $k(\lambda)$ ,  $\mathbf{A}$ ,  $v_*$ , and  $v_{\text{tel}}$  (seven parameters in total). Note that telluric transmittance is simultaneously modeled again when RVs are computed by fitting the template spectrum to individual observed spectra. In fitting each spectral segment, IP is fixed to the one estimated from the corresponding segment of the simultaneously taken LFC spectrum. The optimization of the fitting parameters is performed with the LevenbergMarquardt (LM)  $\chi^2$  minimization technique (e.g., Press et al. 2002), or our customized code of the Markov Chain Monte Carlo (MCMC) samplings (e.g., Hirano et al. 2015); the LM optimization is about twice as fast as the MCMC analysis. For the latter method, we can optionally impose Gaussian priors on some fitting parameters, (e.g., telluric parameters  $\mathbf{A}$  and  $v_{\text{tel}}$ ). Through the analyses of observed spectra, we confirmed that these two optimizations give almost equivalent RV results for nominal targets (slowly rotating M dwarfs), but for stars with moderate rotations ( $v \sin i > 5 \text{ km s}^{-1}$ ) RV results behaved slightly better in the case of the MCMC fitting by imposing telluric priors. This investigation is under progress, and we hope to present the result in future works. For the analyses of observed spectra (Section 5), we present the RV results based on the MCMC analyses. Figure 10 depicts an example of our fitting procedure for a segment (order = 90, part = 17) of an observed IRD spectrum of GJ 699 (blue points).

A total of  $\approx 1000$  segments, from 970 nm to 1700 nm, are analyzed for RV measurements, though a significant fraction ( $> 40\%$ ) of those segments are not usable for RV measurements due to low blaze efficiency around edges of each echelle order and/or very strong telluric lines.

Currently LFC spectra only cover between 1050–1720 nm, thus we are not capable of extracting accurate IPs for spectral segments below  $\approx 1050$  nm. The RV error for each segment is estimated based on the covariant matrix for the LM  $\chi^2$  minimization, or the marginalized posterior distribution of  $v_*$  for the MCMC analysis. The final RV and its uncertainty are determined from the weighted mean of the RV values for all the available (converged) segments after clipping out the segments showing unfavorable behaviors; Segments with an imperfect removal of telluric lines in  $S(\lambda)$  and/or bad estimations of IPs produce anomalistic RV behaviors in comparison with those of the neighboring segments. Those segments are therefore removed in computing the weighted mean for  $v_*$ .

It should be emphasized that our methodology described above relies on the critical assumption that the IP extracted from the LFC spectrum (from the reference fiber) is identical to that of the stellar spectrum (from the stellar fiber); albeit the two fibers (both multi-mode fibers) are identical in shape (circular) and diameter, there is no guarantee that the two fibers produce exactly the same point-spread function on different positions of the detector. One test to verify this assumption is to implement a laboratory experiment with the LFC being injected into both fibers, and check for the magnitude of the “relative” temporal drift between the two fibers. The result of this experiment is presented in detail in Kuzuhara et al. (2018), in which we demonstrated that the relative RV variation between the two LFC spectra is  $1.3 - 1.9 \text{ m s}^{-1}$  including the random Poisson plus readout noise over a time scale of  $\approx 2$  weeks (see Figure 3 of Kuzuhara et al. (2018)). In addition to the fiber-induced difference in IPs, one also needs to account for the different paths which the stellar light and LFC light pass through in the case of on-sky observations; time-variable AO corrections coupled with limited fiber scrambling can lead to a variation in IPs only for stellar spectra, potentially resulting in an apparent shift in stellar RVs. All these concerns motivated us to conduct on-sky observations of several RV standard stars with IRD to quantify the impact of differing IPs for the two IRD fibers. The on-sky stability of stellar RVs is presented in Section 5.

## 4 Validation of the RV Pipeline Based on Mock Spectra

### 4.1 Setups

As the first test of our RV analysis pipeline, we estimated “theoretical” RV precisions that IRD can achieve. To do so, we performed a series of Monte Carlo simulations us-

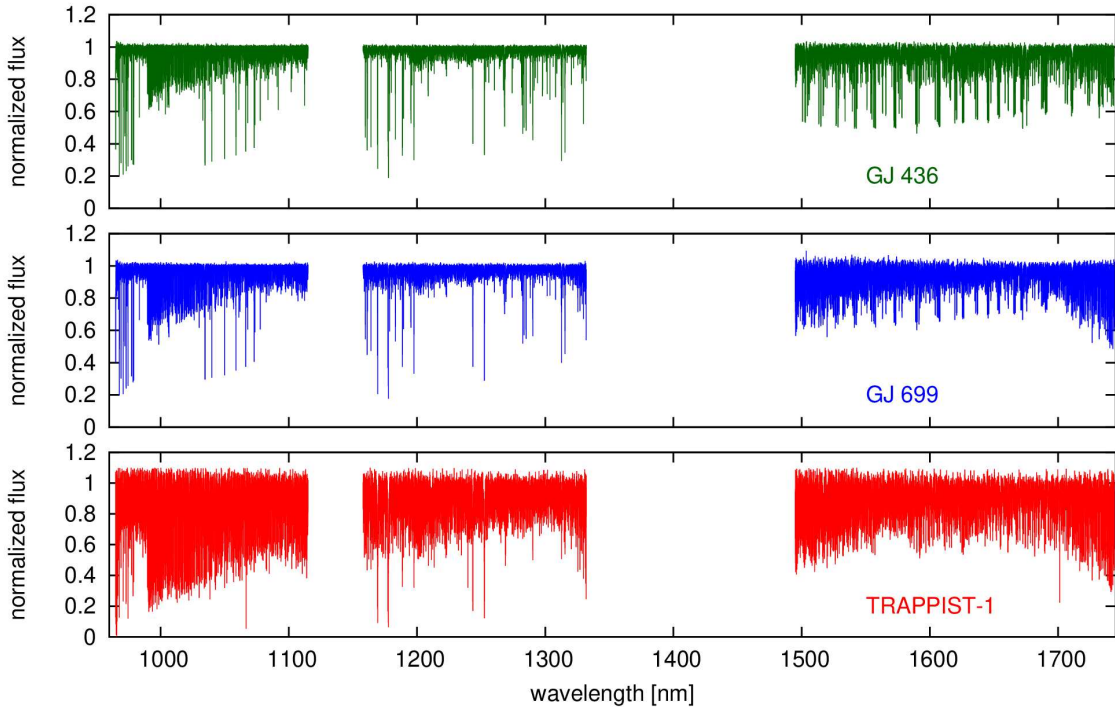


**Fig. 9.** Comparison of the extracted template spectra for three different M dwarfs (GJ 436, GJ 699, and TRAPPIST-1 from top to bottom). The absorption features, between 990 nm and 1050 nm in particular, become deeper for later spectral types.

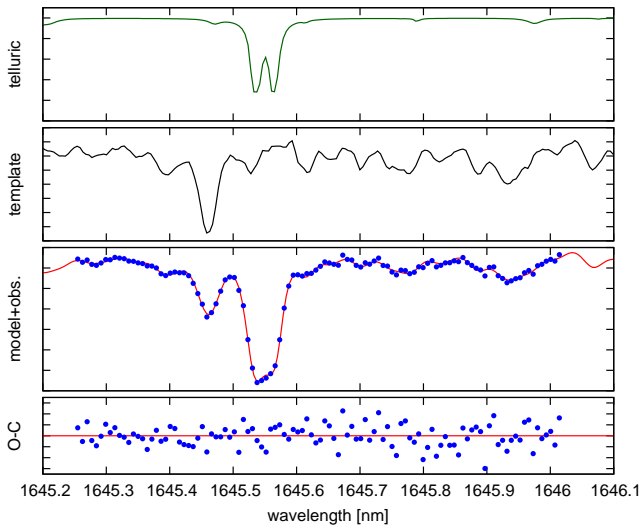


**Fig. 10.** Spectrum fitting by our pipeline for a segment in the  $H$ -band (GJ 699). From top to bottom, the best-fit theoretical telluric transmittance  $T(\mathbf{A}; \lambda)$ , stellar template  $S(\lambda)$ , observed spectrum (plus the best-fit model in red),  $O - C$  residuals are plotted, respectively.

ing theoretical model spectra in the NIR. Although this sort of numerical simulations have been carried out in the past (e.g., Reiners et al. 2010; Rodler et al. 2011), we repeat similar simulations to take into account IRD’s specifications such as the wavelength coverage, spectral resolution, pixel sampling, wavelength-dependent instrumental efficiency, etc. Below, we briefly describe our Monte Carlo simulations to estimate IRD’s RV precisions for each spectral type. The precisions derived here are the uncertainties in  $v_*$  of Equation (2), originating from the Poisson noise (and readout noise) in the stellar spectra as well as the pipeline capability to fit the NIR spectra in the presence of blending telluric lines. In this section, we do not take into account the imperfect removal of telluric lines in the stellar template  $S(\lambda)$  and imperfect estimation of IPs for individual segments. The RV analysis for the actual observed spectra will be presented in Section 5.

We began with a theoretical NIR spectrum generated by the BT-SETTL model (Allard et al. 2013). Here, we adopt three types of M dwarfs and one solar analog: a late M ( $T_{\text{eff}} = 2500$  K), a mid-M ( $T_{\text{eff}} = 3000$  K), an early M ( $T_{\text{eff}} = 3500$  K) dwarfs, and a G dwarf ( $T_{\text{eff}} = 5800$  K). We set the metallicity to  $[\text{Fe}/\text{H}] = 0.0$  for the fiducial case, but we will later use templates with non-solar metallicities to investigate the metallicity dependence of RV precision (Section 4.5). Since RV precisions are known to be

highly dependent on stellar rotation ( $v \sin i$ ), we convolved each PHOENIX spectrum with the rotation plus macroturbulence broadening kernel, following Hirano et al. (2011). For the macroturbulent velocity  $\zeta$  in the radial-tangential model (Gray 2005), we adopted  $\zeta = 1 \text{ km s}^{-1}$  for M dwarfs following Valenti et al. (1998) and Bean et al. (2006), and  $\zeta = 3.98 \text{ km s}^{-1}$  for the solar analog (Valenti & Fischer 2005). We then multiplied the broadened spectrum by the telluric transmission spectrum synthesized by LBLRTM for an arbitrary observing condition on Maunakea (we will also use the observed telluric transmittance in Section 4.6). To simulate IRD observations, this theoretical stellar plus telluric spectrum was multiplied by IRDs wavelength-dependent efficiency, and convolved with the corresponding IP for each segment. The efficiency is based on our observations of a rapid rotator<sup>6</sup>, reflecting the blaze function for each echelle order, fiber transmittance, AO efficiency, detector quantum efficiency, etc. For simplicity, we fixed the IPs for individual segments to the observed ones (extracted by LSD) on an arbitrary night. Finally, the resulting spectral fluxes were converted into the photon counts and stored with exactly the same pixel sampling as IRD’s detector. The Poisson noise was estimated for each pixel by scaling the S/N ratio to the value at a reference wavelength, for which we adopted 1000 nm. We also took into account the readout noise by adding white noise of  $45 \text{ e}^-$  per pixel. This noise level approximately corresponds to the readout noise for a 1-minute integration (i.e., the nominal integration time for GJ 699; Kuzuhara et al. 2018).

The rest of this section presents the simulated results of mock RV analyses, in which we put the mock IRD spectra generated by the above steps into our RV pipeline. Here, the ideal RV precisions of the IRD spectrograph are estimated by focusing on the spectrum fitting procedure in step “C.” of Figure 4. We set the IPs of individual segments to the ones used in creating mock IRD spectra. The adopted stellar template in the RV fit is identical to the input one under the assumption that telluric lines are perfectly removed via the process of extracting the stellar template (step “B.” in Figure 4) using a large number of spectra. We allowed all the seven fitting parameters (including telluric parameters) to vary in the fit.

Figure 11 plots an example of the fitting result for a mock IRD spectrum with  $T_{\text{eff}} = 3000 \text{ K}$ ,  $v \sin i = 1 \text{ km s}^{-1}$ ,  $[\text{Fe}/\text{H}] = 0.0$ , and  $\text{S}/\text{N} \approx 100$  per pixel at 1000 nm, which we call the “fiducial case” in the subsequent analyses. The best-fit RV value, its statistical error, and the reduced  $\chi^2$  value for the fit of each spectral segment are plotted as a function of the central wavelength of the segment, from

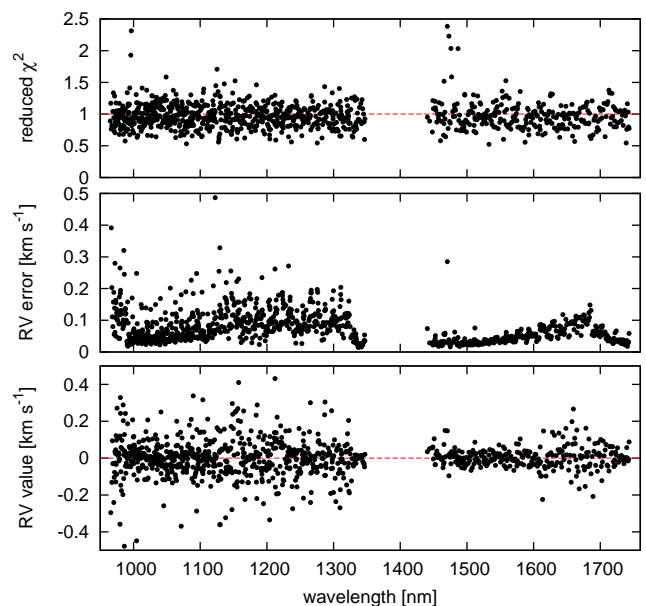


**Fig. 11.** Sample result of the RV analysis for a mock IRD spectrum (fiducial case:  $T_{\text{eff}} = 3000 \text{ K}$ ,  $v \sin i = 1 \text{ km s}^{-1}$ ,  $[\text{Fe}/\text{H}] = 0.0$ ,  $\text{S}/\text{N} \approx 100$  at 1000 nm). RV values (relative to the template), their errors, and reduced  $\chi^2$  are plotted for individual segments, from bottom to top, respectively.

bottom to top, respectively. The absence of data points between 1350 nm and 1450 nm corresponds to the gap between the two IRD detectors. As shown in the figure, the RV precision for each segment is generally better in the  $H$ -band, partly due to higher S/N ratios at longer wavelengths, but the number of segments for the RV fit is larger in the  $Y + J$  bands. Figure 11 includes the fitting results for spectral segments between  $Y$  and  $J$  bands (1113–1160 nm), but since this spectral region is heavily contaminated by strong telluric absorptions, those segments are not used to compute the overall RV precision for each frame. The reduced  $\chi^2$  between the mock spectrum and best-fit model is distributed around 1.0, suggesting a good fit to each segment. A small number of segments ( $\approx 10$ ) show relatively large  $\chi^2$  values ( $\gtrsim 1.5$ ). Those segments are found to have especially strong telluric absorptions, which most likely led to the parameters (and  $\chi^2$ ) captured at a local minimum. Such segments showing anomalies are clipped and ignored in deriving the final RV value from all the segments.

## 4.2 Doppler-shifting the Spectra

Due to the motion of the observer with respect to the barycenter of the solar system, the positions of stellar lines relative to the telluric ones are always shifting in time, implying that the magnitude of blending between stellar and telluric lines is not the same for each spectrum. This time-variable blending of stellar and telluric lines leads to a different level of degeneracy between the stellar RV ( $v_*$ ) and

<sup>6</sup> [http://ird.mtk.nao.ac.jp/IRDpub/index\\_tmp.html](http://ird.mtk.nao.ac.jp/IRDpub/index_tmp.html)

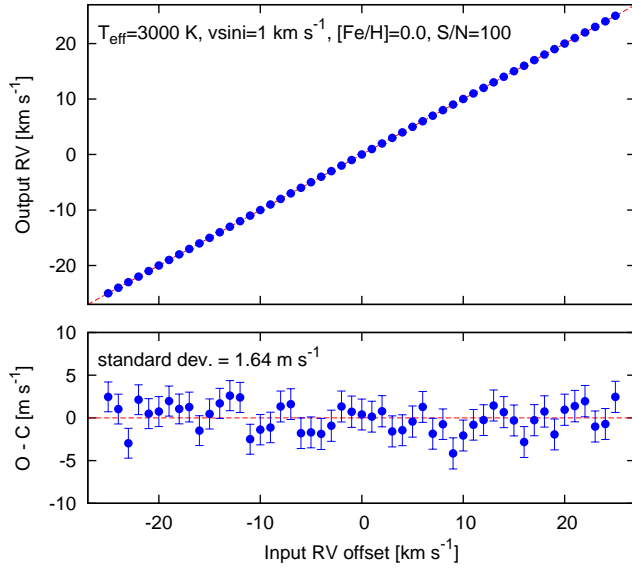


**Fig. 12.** Input RV offset (given to the template) v.s. output RV returned by our pipeline. The bottom panel plots the residual between the input and output RVs in  $\text{m s}^{-1}$ .

telluric parameters in fitting each spectrum, which may cause systematically large scatters in the time sequence of final RVs. Here, in order to check if

1. the RV error returned by our analysis pipeline (i.e., the “internal” error) is consistent with the scatter of RV points calculated through many trials of the mock data analysis, and
2. variations of stellar line positions relative to the telluric line positions have a minor effect on the output RVs,

we generated 51 mock IRD spectra for the fiducial case; We repeatedly Doppler-shifted the input stellar template with the velocity step of  $1 \text{ km s}^{-1}$ , from  $-25 \text{ km s}^{-1}$  to  $+25 \text{ km s}^{-1}$ , simulating a situation that the same target is observed for a whole year around. Note that for simplicity we do not take into account the fact that the stars themselves can have a systemic velocity of up to about  $\pm 50 \text{ km s}^{-1}$  with respect to the Sun.

The result of analyzing the 51 spectra is shown in Figure 12. In the top panel, the output RV values are plotted against the input RV offsets given to the stellar template. The bottom panel of Figure 12 plots the residual between the input and output RVs. The standard deviation of the 51 RV residuals was  $1.64 \text{ m s}^{-1}$ , which is almost consistent with the mean internal error for those points ( $1.80 \text{ m s}^{-1}$ ). In order to investigate the impact of blending between stellar and telluric lines and resultant possible correlation between the input RV and the  $O - C$  residual, we fitted the RV residual by a linear function of the input RV offset, and derived the slope  $\kappa$ . The resulting slope was found to be

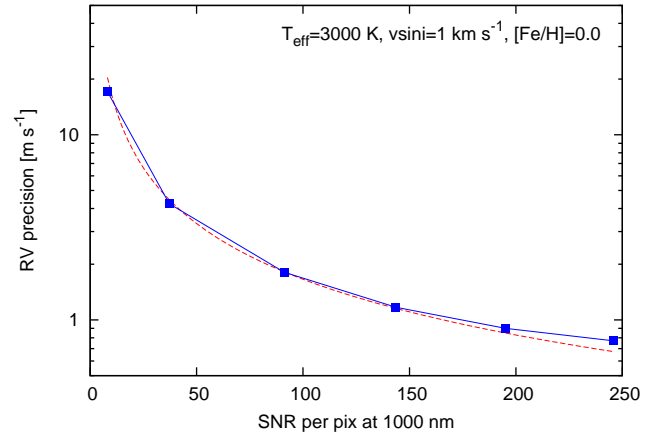


**Fig. 13.** Simulated RV precision as a function of the nominal S/N ratio (Equation 16). The red dashed curve represents the best-fit regression assuming the precision is inversely dependent on the S/N ratio.

$\kappa = -0.019 \pm 0.016 \text{ m s}^{-1} (\text{km s}^{-1})^{-1}$ , consistent with zero within about  $1\sigma$ . All these results imply that the spectral fitting module in our RV-analysis pipeline works well overall, returning RV values and their errors that are almost self-consistent.

### 4.3 S/N Dependence

Next, we checked the dependence of RV precision on S/N ratio of the spectrum. We simulated RV measurements for the fiducial case, but varied the S/N at 1000 nm. We set the counts in the pixel of 1000 nm to  $20^2$ ,  $50^2$ ,  $100^2$ ,  $150^2$ ,  $200^2$ , and  $250^2 \text{ e}^-$  and scaled the flux counts and their Poisson noise for the other pixels. A fixed Gaussian readout noise ( $\text{RN} = 45 \text{ e}^-$ ) was added to each pixel, as in Section 4.2.

Figure 13 plots the internal errors for the RV measurements with different S/N ratios. The horizontal axis in Figure 13 is the “nominal” S/N ratio computed by

$$S/N_{\text{nominal}} = \frac{F(1000 \text{ nm})}{\sqrt{F(1000 \text{ nm}) + \text{RN}^2}}, \quad (16)$$

where  $F(1000 \text{ nm})$  is the flux count in  $\text{e}^-$  at 1000 nm. As expected, the RV precision is almost inversely proportional to the S/N; a regression with  $y = ax^{-1}$  to the result is drawn by the red dashed line in Figure 13. At very high S/N ( $\gtrsim 200$ ), the RV precision is slightly higher than the  $y = ax^{-1}$  curve, suggesting that we have some room for improvement in the RV analysis pipeline; in particular, a higher-order continuum polynomial ( $k(\lambda)$ ) and higher resolution in the convolution (numerical integrations) may be required in Equation (2) for the case of high S/N spectra.

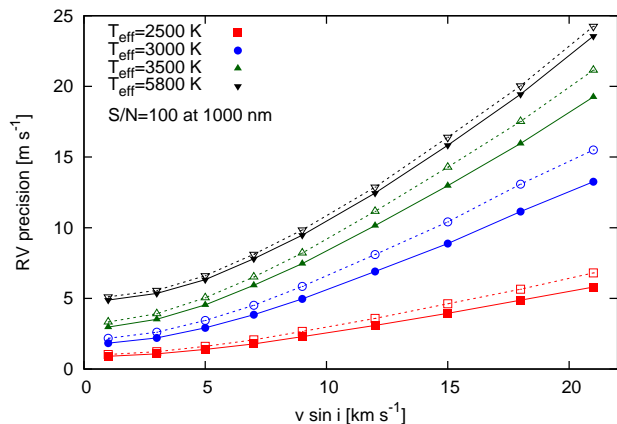


**Fig. 14.** Simulated RV precision as a function of stellar  $v \sin i$  for four different types of stars ( $T_{\text{eff}} = 2500, 3000, 3500, 5800$  K). The solid lines (filled symbols) present the RV precisions when IRD’s whole spectrum is used, while the dashed lines (open symbols) correspond to those if only the wavelength range above 1050 nm (which is covered by the current LFC) is used.

#### 4.4 Dependence on Spectral Type and Rotation Velocity

Spectral type and rotation velocity of the star are the two major components that determine the RV precision. Setting the flux counts to  $100^2 e^-$  at 1000 nm, we created a number of mock IRD spectra for differing spectral types and rotation velocity. We employed four different  $T_{\text{eff}}$  from the BT-SETTL model (Allard et al. 2013) as stated above, and adopted  $v \sin i = 1, 3, 5, 7, 9, 12, 15, 18$ , and  $21 \text{ km s}^{-1}$  for the rotation velocity. In Figure 14, we plot the simulated RV precisions as a function of  $v \sin i$ . Solid lines (filled symbols) show the RV precisions when IRD’s whole spectral range ( $970 \text{ nm} < \lambda < 1744 \text{ nm}$ ) is used for the RV analysis, while dashed lines (open symbols) indicate those for the wavelengths that are currently covered by the LFC spectrum ( $1050 \text{ nm} \lesssim \lambda \lesssim 1730 \text{ nm}$ ). More rapidly rotating stars exhibit worse RV precision due to line-broadening, resulting in less Doppler information, while later-M dwarfs show better RV precisions even for relatively large  $v \sin i$ . This is mainly because late M dwarfs generally have a larger number of molecular lines and deeper features in their spectra, increasing intrinsic Doppler information in the spectra. See Figure 9 regarding how later-type stars exhibit richer features of molecular lines.

For early M dwarfs, we need  $S/N \gtrsim 150$  to achieve a precision of  $< 2 \text{ m s}^{-1}$ , but similar RV precisions are achievable with only  $S/N = 100$  for late-M dwarfs with moderate rotations ( $v \sin i < 8 \text{ km s}^{-1}$ ). The number of absorption lines is much smaller for solar-type stars, which results in limited RV precisions in the NIR (black line in Figure 14); as stated in the literature (e.g., Reiners et al. 2010; Rodler et al. 2011), RV precisions for solar-type stars are much

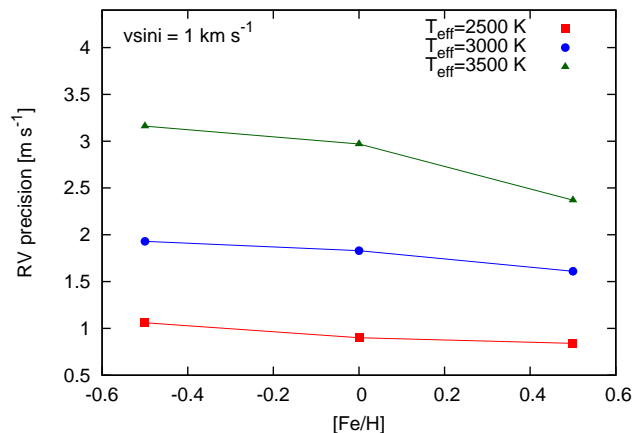


**Fig. 15.** Simulated RV precisions as a function of  $[\text{Fe}/\text{H}]$  for the input stellar templates ( $T_{\text{eff}} = 2500, 3000, 3500$  K,  $v \sin i = 1 \text{ km s}^{-1}$ ,  $S/N \approx 100$  at 1000 nm).

better at optical wavelengths. Meanwhile, RV measurements in the NIR have an advantage over optical measurements in terms of reduced stellar jitter, especially for young stars, due to mitigated contrasts of active regions on the stellar surface (e.g., Beichman et al. 2019).

#### 4.5 Metallicity Dependence

In discussing the occurrence rate of planets revealed by blind RV surveys, one should keep in mind that metal-rich stars have deeper absorption features at all wavelengths and the RV precision tends to be better, facilitating the detection of planets. In order to learn to what extent RV precisions are improved or degraded by stellar metallicity, we repeated the numerical experiment for M dwarfs above with three different metallicities:  $[\text{Fe}/\text{H}] = -0.5, 0.0, +0.5^7$ . In the mock analyses, we adopted  $v \sin i = 1 \text{ km s}^{-1}$  and set the flux count to  $100^2 e^-$  at 1000 nm as in the fiducial case. The result ( $[\text{Fe}/\text{H}]$  v.s. RV precision) is shown in Figure 15. RV precisions were found to be better (worse) for metal-rich (metal-poor) M dwarfs than solar-metallicity stars by 5–20%. One needs to account for the metallicity dependence of RV precision in implementing planet yield simulations for blind Doppler surveys, but our simulated result suggests that the RV precision depends more on the spectral type of the target (i.e., the number of lines) than the metallicity.

#### 4.6 Impact of Telluric Lines

In the mock RV analyses above, we used the theoretical telluric transmittance both in creating mock spectra and

<sup>7</sup> Metal-rich M dwarfs with  $[\text{Fe}/\text{H}] > 0.4$  are very rare, but we test extreme cases here.

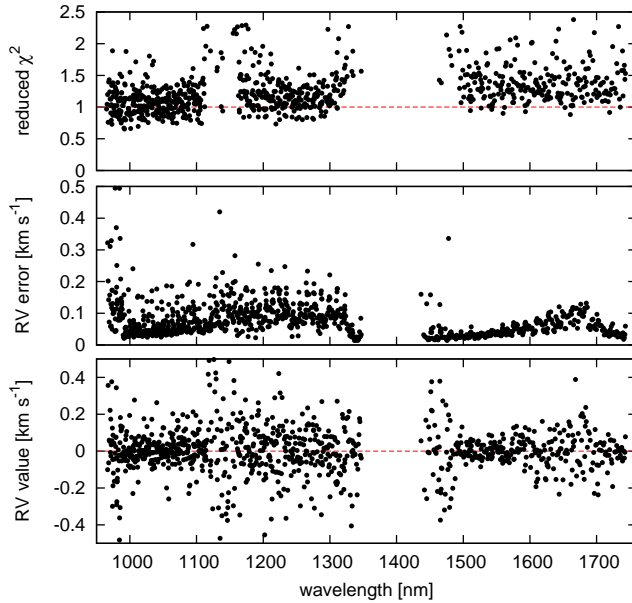


**Fig. 16.** Same as Figure 11 except that we used an empirical telluric transmittance in generating the mock IRD spectra.

fitting the mock data, which corresponds to the ideal cases of our RV measurements with the best achievable precisions. In reality, however, theoretical telluric spectra can disagree with the actual (observed) telluric ones due to incomplete molecular line lists, imperfect input atmospheric profiles, and breaking of approximations used in the theoretical calculations (Rudolf et al. 2016). With a goal of understanding the impact of disagreement between the theoretical and actual telluric transmission spectra on the RV accuracy, we repeated the simulations described in Section 4.2 using “observed” telluric transmission spectra.

Employing the stellar template for the fiducial case, we created 51 mock IRD spectra by Doppler-shifting the template by  $1 \text{ km s}^{-1}$  for each such that the input stellar RV offset ranges from  $-25 \text{ km s}^{-1}$  to  $+25 \text{ km s}^{-1}$ . Instead of multiplying the Doppler-shifted templates by the theoretical telluric transmittance (LBLRTM), we multiplied by an empirical telluric transmittance generated based on the observed spectra of HR 8634 (telluric standard). HR 8634 was observed on several different nights between 2018 June and August; specifically on UT 2018 August 6, this target was visited 6 times during a night so that we can compare telluric spectra taken at different observing conditions (airmass in particular). A total of 96 frames were obtained for this target, covering the airmass range between  $\approx 1.0$  and  $\approx 2.0$ . Since each spectrum of HR 8634 has a limited S/N ratio ( $\approx 150 - 200$  per pixel), which may affect the overall quality of the mock spectra, we randomly combined multiple ( $\approx 5$ ) frames to generate an empirical telluric spectrum for each of the 51 mock data. Although

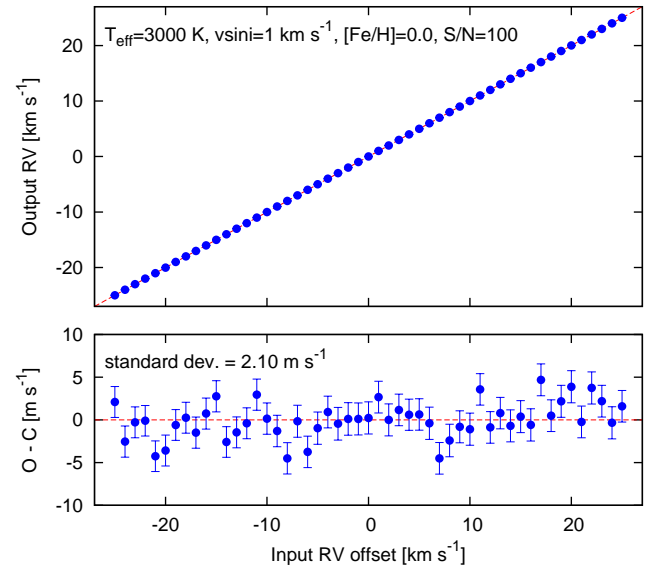


**Fig. 17.** Same as Figure 12 except that we used an empirical telluric transmittance in generating the mock IRD spectra.

this manipulation averages the impact of differing airmass on the telluric lines, the combined empirical spectra still exhibit moderate variations in depth and shape due to different observing conditions. Thus, this numerical experiment also helps us understand the impact of random variations in the observing condition on NIR RV measurements.

Putting these mock IRD spectra into our RV fitting routine, we simulated the RV analysis for the 51 mock spectra. In fitting each mock spectrum, we used the library of “theoretical” telluric transmittance for  $T(\mathbf{A}; \lambda)$  in Equation (2) and optimized the relevant telluric parameters simultaneously with  $v_*$ , mimicking the scenario that we analyze real observed spectra. Figure 16 presents the RV-fit results of individual segments for one of the mock spectra ( $v_* = 0 \text{ km s}^{-1}$ ). When compared with Figure 11, RV values for individual segments (bottom panel) exhibit a larger scatter in Figure 16. In many segments that include strong telluric lines (e.g.,  $1115 \text{ nm} < \lambda < 1165 \text{ nm}$ ,  $1320 \text{ nm} < \lambda < 1495 \text{ nm}$ ), the fits did not converge (reduced  $\chi^2 > 3$ ), or RV values show a very large scatter even in case of convergence. As expected, the reduced  $\chi^2$  values (top panel) in Figure 16 are generally worse than in Figure 11 due to the disagreement between the theoretical and actual telluric lines. Figure 16 indicates that the reduced  $\chi^2$  value is higher in the *H*-band, which is probably related to the fact that for IRD spectra of M dwarfs, S/N ratios are significantly higher in the *H*-band ( $150 - 200$ ) than in the *Y*-band ( $\approx 100$ ), and the same level of fractional disagreements between the theoretical and observed telluric absorptions and/or between the model (polynomial) and observed continuum leads to a larger  $\chi^2$  difference in the

*H*-band.

The output RV values as a function of the input RV offset for the 51 mock spectra are plotted in Figure 17. The bottom panel of the same figure show the residuals between the input and output RVs in  $\text{m s}^{-1}$ . The standard deviation of the residuals was found to be  $2.10 \text{ m s}^{-1}$ , which was larger than that in Section 4.2 by about 28%. The mean internal error returned by the analysis pipeline was  $1.85 \text{ m s}^{-1}$ , suggesting that the disagreement between the theoretical and actual telluric lines indeed produces an additional RV scatter of  $\approx \sqrt{2.10^2 - 1.85^2} = 0.99 \text{ m s}^{-1}$ . In order to check if Doppler-shifts of the template relative to the telluric lines lead to a systematic variation of resulting RVs, we fitted the  $O - C$  residuals in Figure 17 by a linear function of the input RV offset. The best-fit slope was found to be  $\kappa = 0.053 \pm 0.020 \text{ m s}^{-1} (\text{km s}^{-1})^{-1}$ . Given that the theoretical case was consistent with zero (Section 4.2), this result suggests a hint of correlation between relative telluric-line positions and best-fit RV values. The application of our pipeline to real data with telluric absorptions could lead to RV measurements dragged by the positions of telluric lines blended with stellar lines. Fortunately though, the magnitude of RV shifts by the “telluric drag” is only  $\approx \pm 1.3 \text{ m s}^{-1}$  even for the worst cases (RV offset =  $\pm 25 \text{ km s}^{-1}$ ). In addition, post-processing of the RV data may be able to suppress this systematic error in the real data analysis, provided that we have a sufficiently large number of RV points. For reference, when we subtract the best-fit RV trend (slope) in the residuals from the original RVs, the standard deviation becomes  $1.94 \text{ m s}^{-1}$ , almost consistent with the mean internal error.

## 5 Tests of the RV Analysis Pipeline: On-sky Performances

### 5.1 Targets and Analyses

As a last set of tests on our RV analysis pipeline, we analyzed the actual spectra obtained by IRD. The standard stars for RV measurements included GJ 699 (Barnard’s star), which is known to host an exoplanet (Ribas et al. 2018), but since its RV variation by barycenter motion of the star due to the planet is well determined, we can use the star for IRD’s demonstration. We also observed TRAPPIST-1 during the open-use programs (proposal ID’s: S18B-114, UH-37C, UH-37A) between 2018 August and 2019 July (see Hirano et al. 2020). Integration times were set to 45 – 120 sec for GJ 699 and 300 – 1200 sec for TRAPPIST-1, respectively. GJ 699 (Barnard’s star) was observed at three epochs (nights) in 2018 June and four epochs in 2018 August, while TRAPPIST-1 was ob-

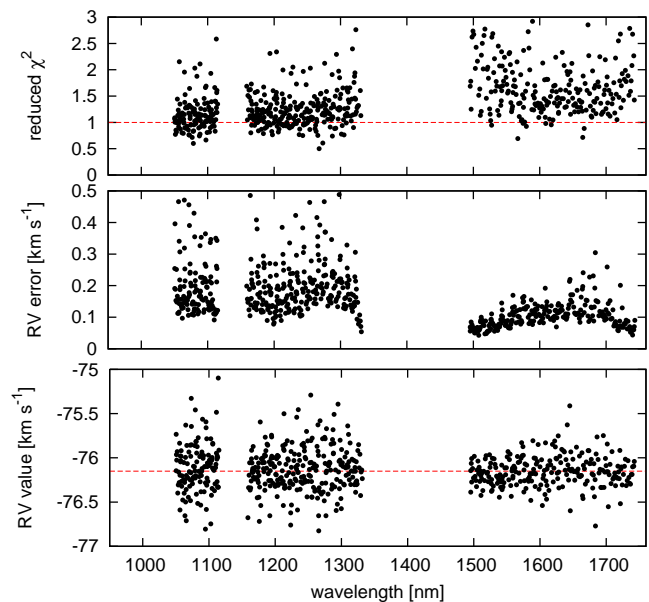


**Fig. 18.** Sample result of the RV analysis for an observed spectrum of TRAPPIST-1. RV values (relative to the template), their errors, and reduced  $\chi^2$  are plotted for individual segments, from bottom to top, respectively.

served at four epochs between 2018 August and 2019 July. The extracted 1D spectra had the S/N ratios of 70 – 180 and 15 – 35 per pixel around 1000 nm for GJ 699 and TRAPPIST-1, respectively. As a telluric standard, we observed HR 8634, which is a B8 star having a featureless spectrum (rapid rotator) and requiring a very short integration time ( $\approx 10 \text{ sec}$ ).

Following the procedure outlined in Figure 4, we first extracted the instantaneous IPs for all the spectral segments between 1050 nm and 1730 nm for each frame, using the LFC spectrum. We then deconvolved each stellar spectrum with those IPs, as well as removed the telluric absorptions by theoretical-model fitting or dividing by the normalized spectrum of the telluric standard star when available. Each deconvolved spectrum was Doppler-shifted to the stellar rest frame based on the cross-correlation between a small telluric-free segment of the spectrum and a theoretical stellar template (BT-SETTL). Checking the barycentric-correction velocity for each frame, we carefully selected a set of frames ( $> 10$  for each target) so that the barycentric motion of Earth leads to the largest range of shifts in stellar line positions with respect to the telluric lines, whose positions are almost constant in time. Those Doppler-shifted frames were eventually median combined to create a high S/N, telluric-free stellar template for each target (Figure 9) to use in the RV analysis (Equation 2).

Putting each stellar spectrum along with corresponding IPs and the stellar template into the RV-fit module of the pipeline, we measured the RVs for individual spectral seg-

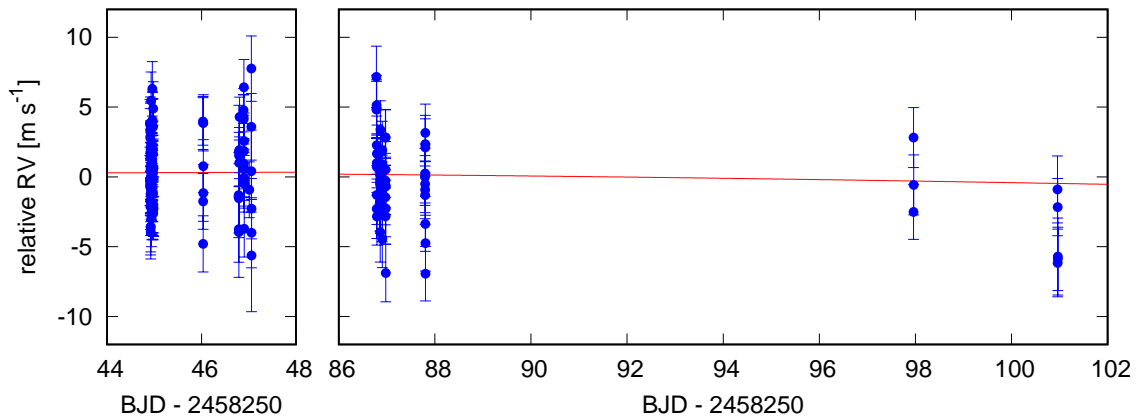


**Fig. 19.** Relative RVs for 176 IRD spectra of GJ 699, analyzed by our pipeline. The red solid line represents the Keplerian orbit of GJ 699b (Ribas et al. 2018).

ments spanning  $\Delta\lambda = 0.7 - 1$  nm. A sample of the RV-fit results (individual segments) for TRAPPIST-1 is presented in Figure 18. As predicted in Section 4.6, the reduced  $\chi^2$  values are generally worse in the  $H$ -band segments most likely due to the disagreement between the observed telluric lines and theoretical telluric spectrum used in the fit. The RV uncertainties returned by the pipeline can be compared with the expected RV precision from numerical simulations for a similar type of star. For the specific frame (ID = 19316) presented in Figure 18, the internal RV error was  $4.98 \text{ m s}^{-1}$  with the S/N ratio being  $\approx 21$  per pixel at 1000 nm, in which the corresponding readout noise is taken into account. Assuming that the temperature and rotation velocity of TRAPPIST-1 are respectively  $T_{\text{eff}} = 2559 \text{ K}$  (Gillon et al. 2017) and  $v \sin i \approx 1.5 \text{ km s}^{-1}$  (Hirano et al. 2020), the expected RV precision according to Figure 14 is  $4.8 - 7.1 \text{ m s}^{-1}$  in case of the solar metallicity, which is fully consistent with the observed one. A total of 176 and 105 frames were analyzed for GJ 699 and TRAPPIST-1, respectively.

## 5.2 RV Result: GJ 699

Figure 19 plots relative RVs of GJ 699 as a function of time; in the plot, the barycentric velocities of Earth were subtracted by using the `TEMPO2` software (Edwards et al. 2006). Given the short integration times, we adopted the central time of the exposure when we computed the barycentric velocity for each frame. About half of the data points (82) were obtained on the night of UT 2018 June 25 (BJD - 2458250  $\approx 45$ ) to check for the RV stability within a single night. The mean internal RV error for the 176 points is  $2.06 \text{ m s}^{-1}$ , while the standard deviation of those RVs was found to be  $2.72 \text{ m s}^{-1}$ . The Keplerian orbit of GJ 699b, reported by Ribas et al. (2018), is drawn

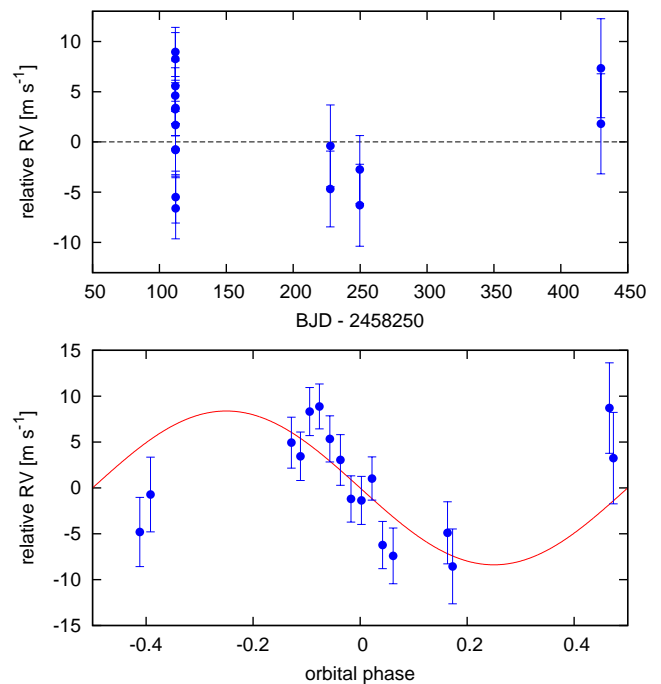


**Fig. 20.** (*Upper*) Observed RVs of TRAPPIST-1 (blue points) as a function of  $\text{BJD}_{\text{TDB}}$ . The RV data on  $\text{BJD} - 2458250 \approx 112$  and 228 were binned so that plotted RV points have similar RV errors ( $3 - 5 \text{ m s}^{-1}$ ). (*Lower*) RVs folded by the orbital period of TRAPPIST-1b ( $P = 1.51087$  days), after subtracting the RV variations for the other six planets expected from the TTV-based masses (Grimm et al. 2018).

by the red solid curve in Figure 19. When we subtract this RV variation by the planet, the standard deviation of the residual becomes  $2.69 \text{ m s}^{-1}$ . The additional scatter of  $\sqrt{2.69^2 - 2.06^2} = 1.73 \text{ m s}^{-1}$  could be ascribed to the effects such as by (1) instrumental instability (in particular, the “relative” drift between the stellar and LFC spectra), (2) stellar activity, and (3) imperfect removal of telluric lines in the stellar template (and telluric drag as described in Section 4.6). The long-term RV stability of GJ 699 measured by IRD will be discussed in more detail in the forthcoming paper (Kotani et al. in prep.). Note that the spectra around  $\text{BJD} - 2458250 \approx 101$  were taken at high airmasses ( $2.5 - 2.8$ ), which might be responsible for a small negative offset seen in Figure 19.

### 5.3 RV Result: TRAPPIST-1

For TRAPPIST-1, the integration times were set to only 5 minutes on UT 2018 August 31 and December 25 in an attempt to observe the Rossiter-McLaughlin effect for this system (Hirano et al. 2020), although we were forced to close the dome of the telescope on December 25 due to very high humidity before the transit started. This small integration time yielded much larger errors and scatters in the individual RV data points than those of the other nights. Hence, we binned the RV points on those two nights so that the RV points after binning have similar uncertainties (1 bin = 7 – 8 frames). The time scale of transits is only 30 – 60 minutes for TRAPPIST-1 planets, so the impact of the Rossiter-McLaughlin effect is averaged out by this binning (i.e., one binned point approximately covers a full transit). The time sequence of TRAPPIST-1’s RV result is presented in the upper panel of Figure 20. The standard deviation of the plotted RV points is  $4.91 \text{ m s}^{-1}$ , while their mean RV error is  $3.18 \text{ m s}^{-1}$ . A part of this additional scatter is definitely ascribed to the gravitational perturbations from the seven planets, but the absence of large systematic RV variations ( $> 10 \text{ m s}^{-1}$ ) suggests that the IRD spectrograph is stable within  $\approx 5 \text{ m s}^{-1}$  on a time scale up to one year.

For reference, we attempted to fit the orbit of TRAPPIST-1b with the current data set. Following Hirano et al. (2020), we fixed the Keplerian orbits of the other six planets (c, d, e, f, g, and h) at the ones expected from the TTV-based masses (Grimm et al. 2018), and fit the RV semi-amplitude  $K$  for planet b only, assuming a circular orbit. The result of the fit is shown in the lower panel of Figure 20, in which the RV points are folded by the period of TRAPPIST-1b. The best-fit RV semi-amplitude was  $K = 8.4 \pm 1.6 \text{ m s}^{-1}$ , which was found to be larger by  $\approx 5 \text{ m s}^{-1}$  than the one expected from TTV ( $\approx 3 \text{ m}$

$\text{s}^{-1}$ : Grimm et al. 2018)<sup>8</sup>. The reason for this disagreement is not known, but apparently the RV data on UT 2018 August 31 (transit night: orbital phase around zero) exhibits a steeper (than expected) slope, as described in Hirano et al. (2020). One reason could be the detector’s persistence and/or imperfect removal telluric lines in the template, but future observations with IRD or other similar spectrographs will settle the issue and enable a precise comparison between the TTV-based masses and RV-based masses. We note that one also needs refined ephemerides for all the planets for the RV determination of accurate planet masses.

## 6 Summary and Discussion

We have described the methodology and pipeline extracting precision RVs from NIR high-resolution spectra, and demonstrated the theoretical and observational performances of the IRD spectrograph, which simultaneously covers  $Y$ ,  $J$ , and  $H$ -bands. To account for the characteristics of the IRD spectrographs (e.g., temporal variations of IPs), we constructed the RV analysis pipeline with a forward-modeling technique, which measures and incorporates the instantaneous variations of telluric lines as well as segment-by-segment IPs. Our numerical simulations using synthetic spectra (BT-SETTL) have shown that for slowly rotating mid-to-late M dwarfs ( $v \sin i < 2 \text{ km s}^{-1}$ ), which are major targets for the blind Doppler survey in the Subaru Strategic Program (SSP: e.g., Kotani et al. 2018), IRD can potentially achieve an RV precision of  $< 2 \text{ m s}^{-1}$  with a moderate S/N ratio ( $\gtrsim 100$  per pixel at 1000 nm). Through the applications of the new pipeline to the observed spectra, we have demonstrated that this level of internal precisions is achieved for bright mid-to-late M dwarfs. The observed RV variation and scatter for GJ 699 are compatible with those reported in the literature (Ribas et al. 2018), although we stress that an additional scatter of  $1 - 2 \text{ m s}^{-1}$  was observed for GJ 699, which could be ascribed to the disagreement between observed and theoretical telluric lines, IRD’s instrumental instability, and/or stellar activity.

The methodology presented in this paper is a first-generation approach to extract precision RVs from IRD spectra, and we emphasize that there is still plenty room for improvement. For instance, in Equation (2), we employ theoretical telluric transmission spectra (LBLRTM) to model each spectrum, but some of the theoretical telluric lines show disagreement from the observed ones, lead-

<sup>8</sup> We confirmed that this result is unchanged even if we fit the raw RV points before binning with the inclusion of the anomalous RVs due to the Rossiter-McLaughlin effect.

ing to possible systematic errors in the extracted RVs, as explained in Section 4.6. A solution to circumvent these systematics is to prepare a set of observed telluric spectra by using rapidly rotating (telluric standard) stars and use those empirical telluric spectra as a library in modeling each stellar spectrum for RV measurement. This in turns requires a large number of observations of telluric standard star(s) to complete various observing conditions (e.g., air-mass, water vapor content of the atmosphere, and seasonal variation of the  $T-p$  profile on Maunakea). A similar approach is explained in Artigau et al. (2014b), who proposed to build a library of absorbances for individual molecular species by the principal component analysis. The library telluric spectra should be free of instrumental broadening, thus requiring the deconvolution of IPs for each observed spectrum of the telluric standard star. To this end, we have been collecting a number of spectra of telluric standard stars, and will continue those observations during the upcoming IRD runs.

One shortcoming of the present technique for RV measurements is that one needs a moderate number of spectra ( $> 10$ ), each of which should preferentially be well separated in terms of observing epochs, to build a high S/N, telluric-free, IP-deconvolved template  $S(\lambda)$ ; with a smaller number of observations ( $< 5$  spectra), one will not be able to obtain accurate RVs due to the imperfect (and/or low S/N) template. This should also be the case for other RV pipelines using forward-modelings (e.g., Zechmeister et al. 2018), since those techniques essentially require multiple observations to disentangle stellar lines from the telluric ones.

Fortunately, stars in the main sequence, M dwarfs in particular, are generally characterized by a relatively small number of stellar parameters (e.g., absolute magnitude  $M_{K_s}$  and  $[\text{Fe}/\text{H}]$ ) and other relevant parameters such as stellar mass and radius (surface gravity) can be derived by empirical relations (e.g., Mann et al. 2015). In addition, the SSP blind Doppler survey for mid-to-late M dwarfs is focusing exclusively on slowly rotating, magnetically inactive stars to achieve good RV precision and accuracy (Kotani et al. 2018). This means that almost all the stars in the survey sample have similar  $v \sin i$ , which should be less than half of the instrumental resolution of IRD (i.e.,  $v \sin i \lesssim 2 \text{ km s}^{-1}$ ). In this case, we might be able to substitute the template for RV measurements of a new target star (for which only a few spectra are available) with another template generated for a similar-type star in terms of  $T_{\text{eff}}$  and  $[\text{Fe}/\text{H}]$ , having a large number of spectra. This attempt to substitute the stellar template is also under progress.

We have focused on RV measurements for spectra ob-

tained by Subaru/IRD, but the techniques and algorithms described in the present paper can be applied to the NIR spectra taken by other Doppler instruments such as CARMENES (Quirrenbach et al. 2016), HPF (Mahadevan et al. 2014), and SPIRou (Artigau et al. 2014a). Those instruments cover different wavelength regions and use different sources of simultaneous wavelength calibration (e.g., a Fabry-Perot based calibration source), but we expect that our pipeline can be applied to those instruments with a moderate level of tuning in relevant parameters and the telluric library. A comparison between the RVs derived by different pipelines would allow us to identify possible systematics in RV measurements and gain insight into the origin of instrumental/telluric/astrophysical correlated noise.

## Acknowledgments

We thank all the members of the IRD consortium for helpful discussions on this project. The data analysis was carried out, in part, on the Multi-wavelength Data Analysis System operated by the Astronomy Data Center (ADC), National Astronomical Observatory of Japan. This work is supported by JSPS KAKENHI Grant Numbers 16K17660, 19K14783, 18H05442, 15H02063, and 22000005, and by the Astrobiology Center Program of National Institutes of Natural Sciences (NINS) (Grant Number AB311017). We are very grateful to the referee, Mathias Zechmeister, for carefully reading our manuscript and providing many insightful comments on our results.

## References

- Allard, F., Homeier, D., Freytag, B., et al. 2013, *Memorie della Societa Astronomica Italiana Supplementi*, 24, 128
- Anglada-Escudé, G., & Butler, R. P. 2012, *ApJS*, 200, 15
- Artigau, É., Kouach, D., Donati, J.-F., et al. 2014a, in *Proc. SPIE*, Vol. 9147, *Ground-based and Airborne Instrumentation for Astronomy V*, 914715
- Artigau, É., Astudillo-Defru, N., Delfosse, X., et al. 2014b, in *Society of Photo-Optical Instrumentation Engineers (SPIE) Conference Series*, Vol. 9149, *Proc. SPIE*, 914905
- Asensio Ramos, A., & Petit, P. 2015, *A&A*, 583, A51
- Astudillo-Defru, N., Forveille, T., Bonfils, X., et al. 2017, *A&A*, 602, A88
- Ballard, S., & Johnson, J. A. 2016, *ApJ*, 816, 66
- Bean, J. L., Seifahrt, A., Hartman, H., et al. 2010, *ApJ*, 713, 410
- Bean, J. L., Sneden, C., Hauschildt, P. H., Johns-Krull, C. M., & Benedict, G. F. 2006, *ApJ*, 652, 1604
- Beichman, C., Hirano, T., David, T. J., et al. 2019, *Research Notes of the American Astronomical Society*, 3, 89
- Bonfils, X., Delfosse, X., Udry, S., et al. 2013, *A&A*, 549, A109
- Butler, R. P., Marcy, G. W., Williams, E., et al. 1996, *PASP*, 108, 500
- Clough, S. A., Shephard, M. W., Mlawer, E. J., et al. 2005, *J. Quant. Spectrosc. Radiat. Transfer*, 91, 233

- Coggins, J. M., Fullton, L. K., & Carney, B. W. 1994, in *The Restoration of HST Images and Spectra - II*, ed. R. J. Hanisch & R. L. White, 24
- Donati, J.-F., Semel, M., Carter, B. D., Rees, D. E., & Collier Cameron, A. 1997, *MNRAS*, 291, 658
- Dressing, C. D., & Charbonneau, D. 2013, *ApJ*, 767, 95
- . 2015, *ApJ*, 807, 45
- Dressing, C. D., Vanderburg, A., Schlieder, J. E., et al. 2017, *AJ*, 154, 207
- Edwards, R. T., Hobbs, G. B., & Manchester, R. N. 2006, *MNRAS*, 372, 1549
- Evans, T. M., Aigrain, S., Gibson, N., et al. 2015, *MNRAS*, 451, 680
- Gaidos, E., Mann, A. W., Kraus, A. L., & Ireland, M. 2016, *MNRAS*, 457, 2877
- Gibson, N. P., Aigrain, S., Roberts, S., et al. 2012, *MNRAS*, 419, 2683
- Gillon, M., Triaud, A. H. M. J., Demory, B.-O., et al. 2017, *Nature*, 542, 456
- Gray, D. F. 2005, *The Observation and Analysis of Stellar Photospheres*
- Grimm, S. L., Demory, B.-O., Gillon, M., et al. 2018, *A&A*, 613, A68
- Hayano, Y., Takami, H., Guyon, O., et al. 2008, *Proc. SPIE*, Vol. 7015, Current status of the laser guide star adaptive optics system for Subaru Telescope, 701510
- Hirano, T., Masuda, K., Sato, B., et al. 2015, *ApJ*, 799, 9
- Hirano, T., Suto, Y., Winn, J. N., et al. 2011, *ApJ*, 742, 69
- Hirano, T., Dai, F., Gandolfi, D., et al. 2018, *AJ*, 155, 127
- Hirano, T., Gaidos, E., Winn, J. N., et al. 2020, *ApJL*, 890, L27
- Jones, A., Noll, S., Kausch, W., Szyszka, C., & Kimeswenger, S. 2013, *A&A*, 560, A91
- Kashiwagi, K., Kurokawa, T., Okuyama, Y., et al. 2016, *Optics Express*, 24, 8120
- Kerber, F., Nave, G., & Sansonetti, C. J. 2008, *Astrophysical Journal Supplement Series*, 178, 374
- Kokubo, T., Mori, T., Kurokawa, T., et al. 2016, in *Proc. SPIE*, Vol. 9912, Advances in Optical and Mechanical Technologies for Telescopes and Instrumentation II, 99121R
- Kopparapu, R. k., Wolf, E. T., Haqq-Misra, J., et al. 2016, *ApJ*, 819, 84
- Kotani, T., Tamura, M., Suto, H., et al. 2014, in *Proc. SPIE*, Vol. 9147, Ground-based and Airborne Instrumentation for Astronomy V, 914714
- Kotani, T., Tamura, M., Nishikawa, J., et al. 2018, in *Proc. SPIE*, Vol. 10702, Ground-based and Airborne Instrumentation for Astronomy VII, 1070211
- Kuzuhara, M., Hirano, T., Kotani, T., et al. 2018, in *Proc. SPIE*, Vol. 10702, Ground-based and Airborne Instrumentation for Astronomy VII, 1070260
- Mahadevan, S., Ramsey, L. W., Terrien, R., et al. 2014, in *Proc. SPIE*, Vol. 9147, Ground-based and Airborne Instrumentation for Astronomy V, 91471G
- Mann, A. W., Feiden, G. A., Gaidos, E., Boyajian, T., & von Braun, K. 2015, *ApJ*, 804, 64
- Noll, S., Kausch, W., Barden, M., et al. 2012, *A&A*, 543, A92
- Pepe, F., Mayor, M., Galland, F., et al. 2002, *A&A*, 388, 632
- Press, W. H., Teukolsky, S. A., Vetterling, W. T., & Flannery, B. P. 2002, *Numerical recipes in C++ : the art of scientific computing*
- Quirrenbach, A., Amado, P. J., Caballero, J. A., et al. 2016, in *Proc. SPIE*, Vol. 9908, Ground-based and Airborne Instrumentation for Astronomy VI, 990812
- Reiners, A., Bean, J. L., Huber, K. F., et al. 2010, *ApJ*, 710, 432
- Ribas, I., Tuomi, M., Reiners, A., et al. 2018, *Nature*, 563, 365
- Rodler, F., Del Burgo, C., Witte, S., et al. 2011, *A&A*, 532, A31
- Rudolf, N., Günther, H. M., Schneider, P. C., & Schmitt, J. H. M. M. 2016, *A&A*, 585, A113
- Sato, B., Kambe, E., Takeda, Y., Izumiura, H., & Ando, H. 2002, *PASJ*, 54, 873
- Tamura, M., Suto, H., Nishikawa, J., et al. 2012, in *Proc. SPIE*, Vol. 8446, Ground-based and Airborne Instrumentation for Astronomy IV, 84461T
- Tennyson, J., & Yurchenko, S. 2018, *Atoms*, 6, 26
- Valenti, J. A., & Fischer, D. A. 2005, *ApJS*, 159, 141
- Valenti, J. A., Piskunov, N., & Johns-Krull, C. M. 1998, *ApJ*, 498, 851
- Zechmeister, M., Reiners, A., Amado, P. J., et al. 2018, *A&A*, 609, A12